



KTH Electrical Engineering

Cluster investigations of the extent and altitude distribution of the auroral density cavity

LOVE ALM

Doctoral Thesis
Stockholm, Sweden 2015

TRITA-EE 2015:100
ISSN 1653-5146
ISBN 978-91-7595-729-6

KTH School of Electrical Engineering
SE-100 44 Stockholm
SWEDEN

Akademisk avhandling som med tillstånd av Kungliga Tekniska högskolan framläggas till offentlig granskning för avläggande av doktorexamen i fysikalisk elektroteknik Fredag, 20 November 2015, klockan 13.15 i Kollegiesalen, Kungliga Tekniska högskolan, Stockholm.

© Love Alm, November 2015

Tryck: Universitetsservice US AB

Abstract

The auroral density cavity constitutes the boundary between the cold, dense ionospheric plasma and the hot, tenuous plasma sheet plasma. The auroral density cavity is characterized by low electron density and particle populations modified by parallel electric fields. Inside the cavity the electron densities can be as much as a factor 100-1000 lower than same altitude outside the cavity.

The Cluster mission's wide range of instruments, long lifetime and ability to make multi-spacecraft observations has been very successful. Over its 15 year lifespan, the Cluster satellites have gathered data on auroral density cavities over a large altitude range and throughout an entire solar cycle, providing a vast data material.

The extent of the density cavity and acceleration region is large compared to the typical altitude coverage of a satellite crossing the cavity. This makes it difficult to produce a comprehensive altitude/density profile from a single crossing. In order to facilitate comparisons between data from different events, we introduce a new reference frame, pseudo altitude. Pseudo altitude describes the satellites' position relative to the acceleration region, as opposed to relative to the Earth. This pseudo altitude is constructed by dividing the parallel potential drop below the satellite with the total parallel potential drop. A pseudo altitude of 0 corresponds to the bottom of the acceleration region and a pseudo altitude of 1 to the top of the acceleration region.

As expected, the pseudo altitude increases with altitude. The electron density exhibits an anti-correlation with the pseudo altitude, the density becomes lower close to the upper edge of the acceleration region. The upper edge of the acceleration region is located between a geocentric altitude of 4.375 and 5.625 R_E . Above the upper edge of the acceleration region, the electron density continues to decrease for the entire range of the study, 3.0-6.5 R_E . This is much further than the geocentric altitude range of 2-3 R_E which is suggested by previous models. We can conclude that the auroral density cavity is not confined by the auroral acceleration region, as suggested by previous models, and may extend all the way to the plasma sheet.

Sammanfattning

Densitetskaviteten utgör ett gränsskikt mellan det kalla, täta, jonofärska plasmat och det varma, tunna, plasmat från plasma sheet. Densitetskaviteten karakteriseras av en låg elektrontäthet och partikelpopulationer som modifierats genom acceleration av parallell elektriska fält. Inne i densitetskaviteten kan elektrontätheten vara en faktor 100–1000 lägre än på samma höjd utanför kaviteten.

Clustersatelliternas kombination av en mångsidig instrumentering, lång livstid och förmåga till simultana observationer med flera satelliter har gjort dem mycket framgångsrika. I 15 års tid har Cluster samlat in data från densitetskaviteter över ett stort höjdiintervall och under en hel solcykel, vilket resulterat i ett omfattande datamaterial.

Densitetskavitets höjdstreckning är mycket större än den typiska höjdtäckningen för en satellitpassage. Därför är det svårt att åstadkomma tillräcklig omfattande höjd-/densitetsprofil från en enskild satellitpassage. För att underlätta jämförelser mellan data från olika satellitpassager så introducerar vi en alternativt referenssystem, pseudohöjd, där satellitens position beskrivs relativt accelerationsområdet, istället för relativt jorden. Pseudohöjden konstrueras genom att dela det parallella potentialfallet nedanför satelliten med den totala parallella potentialfallet. Det leder till att botten på accelerationsområdet motsvaras av pseudohöjd 0 och toppen på accelerationsområdet av pseudohöjd 1.

Som förväntat ökar pseudohöjden med den geocentriska höjden. Elektron-tätheten är anti-korrelerad med pseudohöjden, den lägsta elektron tätheten uppmäts nära toppen av accelerationsområdet. Accelerationsområdets övre gräns återfinns mellan 4.375 och 5.625 R_E . Ovanför accelerationsområdet så försätter elektrontätheten att minska inom det område som studerats, 3.0–6.5 R_E . Detta är avsevärt högre än den höjdstreckning på 2–3 R_E som tidigare modeller ger. Vi drar slutsatsen att densitetskaviteten inte är ett fenomen som är begränsat till accelerationsområdet, vilket tidigare modeller antyder, och eventuellt sträcker sig ända till plasma sheet.

Acknowledgements

The process of writing a thesis can feel like a solitary experience, but your research never just your own. It is the work of everyone who studied the subject before you, everyone who disagreed with you, everyone who offered you advice, everyone who lauded you, everyone who criticized you, and of everyone who may come to wield its results. There are many people who have played a part in the thesis you hold in your hand today...

... my supervisor Göran Marklund for giving me such free reins in my research for allowing me to set my own course, make my own mistakes, find my own solutions and help me back on track when I got too carried away. And for showing that the academic lifestyle can include ditching conference lectures for taking long bike rides, or going kayaking on a weekday.

... my co-supervisor Tomas Karlsson for always being able to provide a fresh perspective on things and for seeing the details that makes the difference.

... my co-workers at the department for new ideas, new perspectives and when needed poking holes in the mist of confusion and clouds of introspection shrouding my head.

... Andris Vaivads and Yuri Khotyaintsev at IRF in Uppsala for their work with developing the IRFU Matlab package and making it available to the community. Without it I would have struggled with making visualizations, not coming to realizations.

... my fellow students at UNIS in Longyearbyen and Barrack 3, my home away from home. You made five weeks of perpetual darkness and hard work seem like vacation in the sun. Until we meet again.

... my family for being a fixed point in the life for a science vagabond.

... my grandmother Ruth Alm, who never got to experience this day. She was probably more enthusiastic about my upcoming graduation than anyone else.

... LoST, my coterie of friends, coconspirator and trustworthy characters, keeping me off the straight and narrow.

... Beate Behnke for allowing me to use her amazing photo of the aurora.

... and you who are reading this. Because the process does not end when ideas have become printed words. It begins when printed words become new ideas.

Science is not a noun

Science is can not be held in your hand or stored on a shelf

Science is not our accumulated knowledge

Science is the process through which we accumulate knowledge

Science is answering questions and questioning answers

Science is a verb

Contents

Contents	vi
List of Papers	ix
List of Figures	x
List of Tables	xi
1 Introduction	1
2 Space plasma physics	3
2.1 Single particle motion	4
2.2 Magnetohydrodynamics	7
3 Auroral physics	9
3.1 The Sun and Solar Wind	9
3.2 The Magnetosphere	11
3.3 The Ionosphere	13
3.4 Auroral current system	16
3.5 The substorm cycle	16
3.6 The Auroral Density Cavity	18
3.7 The Auroral Acceleration Region	20
4 The Cluster Mission	23
4.1 Cluster Ion Spectrometry	24
4.2 Electric Field and Waves	26
4.3 Fluxgate Magnetometer	27
4.4 Plasma Electron And Current Experiment	27
4.5 Waves of HIGH frequency and Sounder for Probing of Electron density by Relaxation	29
5 Methodology	31
5.1 High resolution electron density measurements	31

<i>CONTENTS</i>	vii
5.2 Estimating parallel electric fields	32
5.3 Determining the satellite's position relative to the auroral acceleration region	34
5.4 Estimating currents	36
6 Results	39
7 Discussion and Conclusions	45
Bibliography	51

List of Papers

This thesis is based on the following publications

1. **L. Alm**, G. T. Marklund, T. Karlsson, and A. Masson. 2013. Pseudo altitude: A new perspective on the auroral density cavity. *Journal of Geophysical Research: Space Physics*. ISSN: 2169-9402. URL: <http://dx.doi.org/10.1002/jgra.50408>.
2. **L. Alm**, G. T. Marklund, and T. Karlsson. 2014. In situ observations of density cavities extending above the auroral acceleration region. *Journal of Geophysical Research: Space Physics*, ISSN: 2169-9402. URL: <http://dx.doi.org/10.1002/2014JA019799>.
3. **L. Alm**, B. Li, G. T. Marklund, and T. Karlsson. 2015. Statistical altitude distribution of the auroral density cavity. *Journal of Geophysical Research: Space Physics*, 120(2):996–1006. ISSN: 2169-9402. URL: <http://dx.doi.org/10.1002/2014JA020691>.
4. **L. Alm**, G. T. Marklund, and T. Karlsson. 2015. Electron density and parallel electric field distribution of the auroral density cavity. *Journal of Geophysical Research: Space Physics (forthcoming)*

The papers have been reprinted with permission from their copyright holder.

Publications by the author not included in this thesis:

B. Li, G. Marklund, **L. Alm**, T. Karlsson, P.-A. Lindqvist, and A. Masson. 2014. Statistical altitude distribution of cluster auroral electric fields, indicating mainly quasi-static acceleration below $2.8 R_E$ and Alfvénic above. *Journal of Geophysical Research: Space Physics*, 119(11):8984–8991. ISSN 2169-9402. URL <http://dx.doi.org/10.1002/2014JA020225>. 2014JA020225.

List of Figures

2.1	Examples of particle drift motions	6
3.1	The solar magnetic field throughout the solar cycle	10
3.2	The heliospheric magnetic field	10
3.3	The Earth's magnetosphere	12
3.4	Ionospheric ion and neutral composition	14
3.5	Generation of Pedersen and Hall currents	14
3.6	Pedersen and Hall currents as a function of altitude	15
3.7	The current systems of the auroral oval	17
3.8	Cartoon of the Dungey cycle	18
3.9	Cartoon illustrating the closure of the substorm current wedge through the ionosphere	19
4.1	Orbit of the Cluster constellation	24
5.1	The curlometer method	37
6.1	Summary plot of the electron density as a function of geocentric altitude	40
6.2	Summary plot of the electron density as a function of pseudo altitude .	40
6.3	Electron density versus local pseudo altitude	41
6.4	Summary plot showing C1 crossing the upper edge of the AAR	42
6.5	Summary plot of statistical extent and distribution of the auroral density cavities	43
7.1	Model of the density cavity based on the statistical data	47
7.2	Distribution of electron and ion energy as a function of geocentric altitude	48

List of Tables

4.1	Summary of the operational history of CIS instruments	25
4.2	Summary of FGM operating ranges and resolutions	27
4.3	Summary of the operational history of PEACE instruments	28

Chapter 1

Introduction

The nocturnal displays of light known as the aurora borealis or aurora australis have fascinated people throughout the ages. Their ghostly appearance, often regarded as omens, wove them into the fabric of myth and religion. In Norse mythology the aurora was considered to be one of the incarnations of Bifrost, the bridge that linked Midgard, the realm of men, with Asgard, the realm of the Aesir. The Finnish word for aurora is, Revontulet (fox fire), which comes from folklore where the aurora is attributed to sparks flying from a fox's tail as it runs across the snow. While our current understanding, that aurora is caused by electrons impacting the atmosphere, is more mundane, the lights themselves are no less enchanting for a modern spectator.

Despite its longstanding place in myths and folklore, it would take until the seventeenth century before the first attempts to truly understand the aurora. Galileo Galilei, who is often accredited for the expression aurora borealis, believed that the aurora was caused by sunlight being reflected by air rising out of the Earth's shadow. The French, priest, astronomer, and mathematician Pierre Gassendi concluded that the aurora must occur at a great altitude since it appeared identical even when viewed from distant locations. In 1731, the French astronomer, and geophysicist Jean-Jacques d'Ortous de Mairan suggested that the occurrence of the aurora was related to the solar atmosphere, since the low auroral activity during the latter half of the seventeenth century and early eighteenth century was correlated with the extremely low number of sunspots. One of the first scientists to make the connection between the aurora and the Earth's magnetic field was the Swedish astronomer Anders Celsius. In one of his earliest works, published in 1733, *Observations of the Aurora Borealis in Sweden*, he reported on the influence the aurora had on the compass needle.

Despite many technological breakthroughs, many of the original methods for observing the aurora are still important tools in this day and age. Visual observations, though by camera and photography rather than the eye and hand drawn sketches, allows us to see the footprint of auroral processes originating far away from

the Earth. Ground based magnetometer chains allow us to monitor the constant fluctuations of the geomagnetic field in response to the Sun's activity. In addition, we now have ground based radar system, such as EISCAT and SuperDarn which can study the properties of the auroral ionosphere.

The introduction of satellite missions for studying auroral phenomena has been a major advancement by offering the opportunity to study physics driving the aurora right at the source. The main drawback is that satellites are in constant motion and follow fixed orbits in space. A satellite can never stay in place and give long term data and it is too costly to have enough satellites in orbit for continuous coverage of a specific region. The combination of long term ground based observation and in-situ satellite observations has allowed us to get the best of two worlds.

For the past four years, my research has focused on studying one particular aspect of the auroral region, the auroral density cavity, using data from the four Cluster satellites.

Chapter 2

Space plasma physics

A plasma is a gas with a significant degree of ionization. This makes plasma susceptible to both the regular gas laws and those of electromagnetics. Compared to the other three states of matter, gas, liquid, and solid, plasma is relatively uncommon here on Earth. While it can be found in things such as lightning bolts, fires and neon signs it is not something we have an intuitive understanding of. But from a cosmological perspective, plasma is the most common state in the universe. In fact, the vast majority of all visible objects in the universe consist of plasma, covering a wide range of temperatures and densities.

One often used definition of plasma is that it is quasi-neutral and exhibits collective behavior (Chen, 2006). In a vacuum, the electric field from a charged probe will decrease with the square of the distance, but will not vanish even at great distances. If we insert two oppositely charged probes into a plasma, the positive probe will attract electrons and the negative probe attract (positively charged) ions. The particles will shield out the electric field and outside this cloud of attracted particles the potential negligible. For a plasma consisting of a Maxwellian ion and electron distribution, the potential as a function of the distance to the probe can be described by,

$$\phi = \phi_0 \exp(-|x|/\lambda_d), \quad (2.1)$$

where ϕ is the electric potential, ϕ_0 is the electric potential at the origin, x the distance from the origin and λ_d is the debye length. The debye length is the characteristic length scale over which the electric potential is shielded out and is defined as,

$$\lambda_d \equiv \sqrt{\frac{\epsilon_0 k_B T_e}{ne^2}}, \quad (2.2)$$

where ϵ_0 is the permittivity of vacuum, k_B is Boltzmann's constant, T_e is the electron temperature, n the electron density and e the elementary charge. For a plasma in which the characteristic length scale is much larger than the debye length,

the plasma can be considered to be quasi-neutral. This implies that the electron density and ion density are roughly equal and electric fields cannot propagate over distances much larger than the debye length.

2.1 Single particle motion

A charged particle in a magnetic and electric field is subject to the Lorentz force, \mathbf{F}_L , which can be described as,

$$\mathbf{F}_L = q(\mathbf{E} + \mathbf{v} \times \mathbf{B}), \quad (2.3)$$

where q is the charge of the particle, \mathbf{E} is the electric field, \mathbf{v} the velocity of the particle and \mathbf{B} the magnetic field. The effect of the electric field is easy to visualize, a positively/negatively charged particle is accelerate parallel/antiparallel to the electric field. Since the $\mathbf{v} \times \mathbf{B}$ force is perpendicular to the velocity vector, it does not change the magnitude of the velocity but rather the direction of the velocity. The Lorentz force causes the charged particles to gyrate in the plane perpendicular to the magnetic field, the so called cyclotron motion. The cyclotron frequency, ω_c is defined as,

$$\omega_c = \frac{|q|v_{\perp}^2}{m}, \quad (2.4)$$

where q is the charge of the particle, m is the mass of the particle and v_{\perp}^2 the perpendicular velocity of the particle. The radius of a charged particle's orbit around the magnetic field line, the Lamour radius, r_L , is defined as,

$$r_L = \frac{mv_{\perp}^2}{|q|B}. \quad (2.5)$$

It is worth noting that both the cyclotron frequency and the Lamour radius are mass dependent. Therefore, the large mass difference between electrons and ions will cause them to gyrate over very different time and length scales.

Guiding center drifts

The combination of a magnetic field and an external force, which is perpendicular to the magnetic field, introduces considerably more complicated orbits. As can be seen in Figure 2.1, as the particle is accelerated by the external force changes the gyro radius, causing the gyro center to drift in the perpendicular direction. The drift velocity of the gyro center, \mathbf{v}_d can be described as,

$$\mathbf{v}_d = \frac{1}{q} \frac{\mathbf{F} \times \mathbf{B}}{B^2}, \quad (2.6)$$

where \mathbf{F} is the external force. for example the electric force, $q\mathbf{E}$, and the gravitational force, mg . It is worth noting that the electric force does not introduce a

net current, as the electrons and ions gyrate in opposite directions but also gain energy in opposite directions, resulting in that they drift in the same direction. However, the drift motion due to gravitational force will result in a net current, as electrons and ions drift in opposite directions. In addition, non-uniform electric fields introduce similar drift motions due to the variations in the gyro radius due to varying electric field strength. For a non-uniform electric field the drift velocity, $\mathbf{v}_{\nabla E}$, can be written as,

$$\mathbf{v}_{\nabla E} = \left(1 + \frac{1}{4}r_L^2 \nabla^2\right) \frac{\mathbf{E} \times \mathbf{B}}{B^2}, \quad (2.7)$$

where ∇ is the vector differential operator. Similarly, for a non-uniform magnetic field, the drift velocity, $\mathbf{v}_{\nabla B}$, can be written as,

$$\mathbf{v}_{\nabla B} = \pm \frac{1}{2}v_{\perp}r_L \frac{\mathbf{E} \times \nabla \mathbf{B}}{B^2}. \quad (2.8)$$

The $\nabla \mathbf{B}$ drift causes charge separation and will therefore introduce a net current.

Magnetic mirroring

The gyro motion of a charged particle, around the magnetic field line, gives the particle a magnetic moment. The magnetic moment is generally considered to be an adiabatic invariant; it is constant as long as the magnetic field changes over a time scale much longer than the gyro period. This can be described as,

$$\mu = \frac{1}{2} \frac{mv_{\perp}^2}{B}, \quad (2.9)$$

where μ is the magnetic moment. A typical example of a particle which follows the first adiabatic invariant is an electron precipitating along the magnetic field. As the magnetic field converge, and the magnetic field strength increase, the perpendicular velocity must increase in order to conserve the magnetic moment. This can be described as,

$$\frac{1}{2} \frac{mv_{\perp 0}^2}{B_0} = \frac{1}{2} \frac{mv'^2_{\perp}}{B'}, \quad (2.10)$$

where the superscript ' denotes a arbitrary point along the magnetic field line and the subscript 0 denotes the point of origin. Since the total energy of the particle must be conserved, this can only be achieved by a conversion of parallel velocity into perpendicular velocity. This can be described as,

$$v'^2_{\perp} + v'^2_{\parallel} = v^2_{\perp 0} + v^2_{\parallel 0} \equiv v_0^2. \quad (2.11)$$

If the magnetic field grows strong enough, the particle will reach zero parallel velocity and be unable to continue along the magnetic field line. This causes the

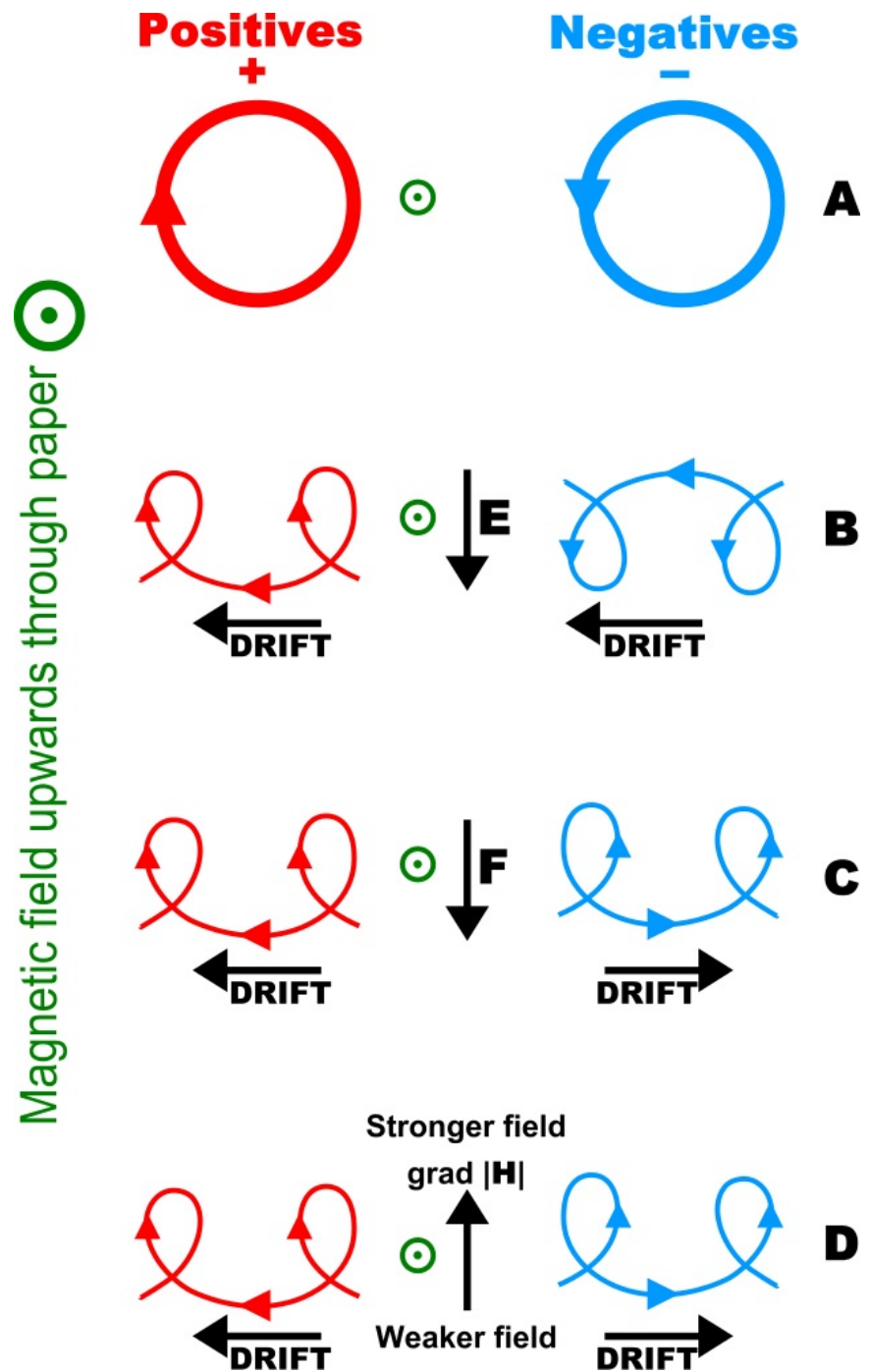


Figure 2.1: Examples of particle drift motions. Adapted from Alfvén (1950); Ian Tresman, Wikimedia Commons

particle to be reflected back towards the region of weaker magnetic field, so called magnetic mirroring. The mirroring condition can be described as,

$$\frac{B_0}{B'} = \frac{v_{\perp 0}^2}{v_{\perp}'^2} = \frac{v_{\perp 0}^2}{v_0^2} \equiv \sin^2(\theta_m) \quad (2.12)$$

where θ_m is the pitch angle for mirroring. The smaller the pitch angle of a particle, the stronger the magnetic field will have to be for the particle to mirror. If we replace B with B_m , the maximum magnetic field in the mirror region, we can estimate the critical pitch angle which indicates the lowest pitch angle which eventually will lead to reflection. This is called the loss cone angle, θ_{LC} , as the critical angle encloses a cone in velocity space. This can be seen on closed field lines in the Earth's magnetosphere where particles become trapped between their mirror points in opposite hemispheres. However, particles which are located inside the loss cone will escape the mirror region and be lost in the ionosphere.

2.2 Magnetohydrodynamics

When studying macroscopic plasmas, with a large number of particles, the equations describing single particle motions can become too unwieldy. In addition to external electric and magnetic fields, the motion of the particles will generate their own magnetic and electric field, creating a continuous feedback loop. A good description of a plasma must be able to describe this feedback cycle in a self consistent fashion. An alternative approach to solving the motion of each particle using the single particle equations is to treat the plasma as a conductive fluid. This approach, which was pioneered by Hannes Alfvén, is known as magnetohydrodynamics (MHD). By assuming that the system's spatial scale is large compared to the ion gyro radius and the debye length, and that the time scale is large compared to the period of the cyclotron motion, we can average out the motions of individual particles and rely on the bulk motion of the plasma.

The fluid description of each particle species relies on six equations: Maxwell's four equations, the continuity equation and the momentum equation. Maxwell's equations describe the relation between electric charge, electric fields, currents and magnetic fields. In their differential form they can be written as,

$$\nabla \cdot \mathbf{E} = \frac{\rho}{\epsilon_0}, \quad (2.13)$$

$$\nabla \cdot \mathbf{B} = 0, \quad (2.14)$$

$$\nabla \times \mathbf{E} = -\frac{\partial \mathbf{B}}{\partial t}, \quad (2.15)$$

$$\nabla \times \mathbf{B} = \mathbf{j} + \epsilon_0 \frac{\partial \mathbf{E}}{\partial t}, \quad (2.16)$$

where ρ is the charge density and \mathbf{j} the current density. The continuity equation states that the number of particles, excluding sources and losses, is defined as,

$$\frac{\partial n_j}{\partial t} + \nabla \cdot (n_j \mathbf{v}_j) = 0 \quad j = i, e. \quad (2.17)$$

The momentum equation can be written as,

$$m_j n_j \left[\frac{d\mathbf{v}_j}{dt} + \mathbf{v}_j \cdot \nabla \mathbf{v}_j \right] = q_j n_j (\mathbf{E} + \mathbf{v}_j \times \mathbf{B}) - \nabla p_j \quad j = i, e. \quad (2.18)$$

By combining the momentum equation for the ions and electrons we can formulate a generalized Ohm's law,

$$\mathbf{E} + \mathbf{v} \times \mathbf{B} = \eta \mathbf{j} + \frac{1}{ne} \mathbf{j} \times \mathbf{B} - \frac{1}{ne} \nabla \cdot \mathbf{P}_e + \frac{m_e}{ne^2} \left[\frac{\partial \mathbf{j}}{\partial t} + \nabla (\mathbf{j} \mathbf{v} + \mathbf{v} \mathbf{j}) \right], \quad (2.19)$$

where \mathbf{P}_e is the full pressure tensor. The generalized Ohm's law consists of four terms, the first relates to the collisional resistivity, the second to the Hall effect, the third to pressure gradients and the fourth to effects from electron inertia.

A typical plasma in space is essentially collisionless which allows us to ignore the resistivity term. The Hall term scales with the ratio between the characteristic length scale of the plasma, L_c , and the ion inertial length, λ_i , and can be safely ignored for length scales $L_c \gg \lambda_i$. The pressure term can be ignored if the gradients are small over the characteristic length scale of the plasma. The last term scales with the electron inertial length and can be ignored if $L_c \gg \lambda_e$. If these four conditions are fulfilled, as is often the case in space, we have what is known as ideal MHD,

$$\mathbf{E} + \mathbf{v} \times \mathbf{B} = 0. \quad (2.20)$$

This is also known as the frozen-in field condition. The consequence is that the motion of the magnetic field lines follows the motion of the plasma. Ideal MHD is generally valid for many of the large scale processes of the magnetosphere but breaks down in several important regions. The frozen-in condition prevents plasma transport across magnetic boundaries and changes in the magnetic topology, i.e. magnetic reconnection, an important process which will be discussed in Section 3.5. An additional consequence is that it forbids the formation of electric fields which are parallel to the magnetic field, a characteristic feature of the auroral acceleration region, which will be discussed further in Section 3.7.

Chapter 3

Auroral physics

3.1 The Sun and Solar Wind

The Sun possesses a magnetic field which is produced internally by the convection and rotation of the plasma in the convection zone. The Sun has a differential rotation where the equatorial region rotates faster than the polar region. At the equator the rotational period is 25.05 days, whereas it at the poles is 34.4 days (Williams, 2015). Since solar plasma is highly conductive, the magnetic field lines follow the frozen-in condition. As can be seen in Figure 3.1, this causes the magnetic field line to slowly wind up around the sun, transforming from a primarily poloidal magnetic field to a more torodial configuration. This accumulation of magnetic flux is the driving force behind solar flares and coronal mass ejections. They serve to release the stored magnetic energy and return the magnetic field to a more poloidal configuration. This accumulation and release of magnetic energy is the cause of the 11-year solar cycle, where the number of sunspots is correlated with the solar activity.

Part of the solar plasma escapes the Sun in the form of the solar wind. The solar wind can be divided into two different categories, the slow and the fast solar wind. The slow solar wind originates at high latitudes and is characterized by a speed of 400 km/s and a temperature of $1.2\text{--}1.4 \cdot 10^6$ K, whereas the fast solar wind originates in the equatorial plane and is characterized by a speed of 750 km/s and a temperature of $5 \cdot 10^5$ K (Feldman *et al.*, 2005) The composition of the solar wind is approximately 95 % ionized hydrogen, with 5 % ionized helium and trace amounts of heavier elements (Kivelson and Russell, 1995).

Since the solar wind plasma has a very high conductivity, the frozen-in condition applies. As can be seen in Figure 3.2a, this results in that the radial motion of the solar wind stretches the magnetic field lines along the equatorial plane, forming two regions of opposing magnetic fields and a current sheet separating the two regions. At the same time the rotation of the Sun causes the foot points of the magnetic field lines to move relative to the plasma, causing the magnetic field

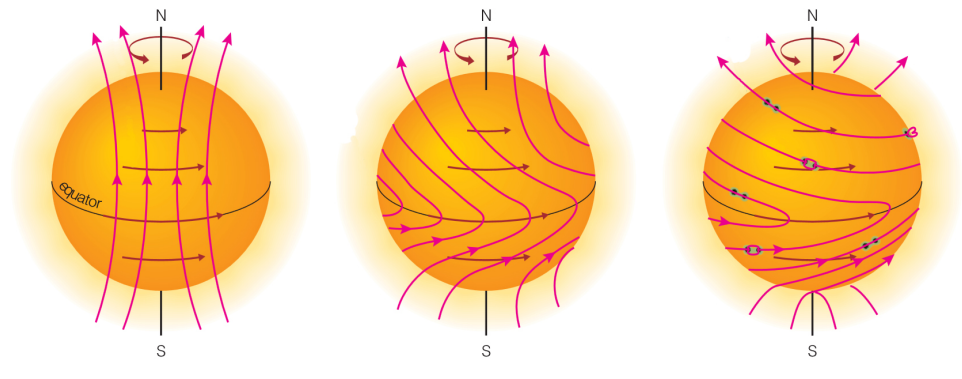


Figure 3.1: The solar magnetic field throughout the solar cycle. Adapted from Bennet *et al.* (2008)

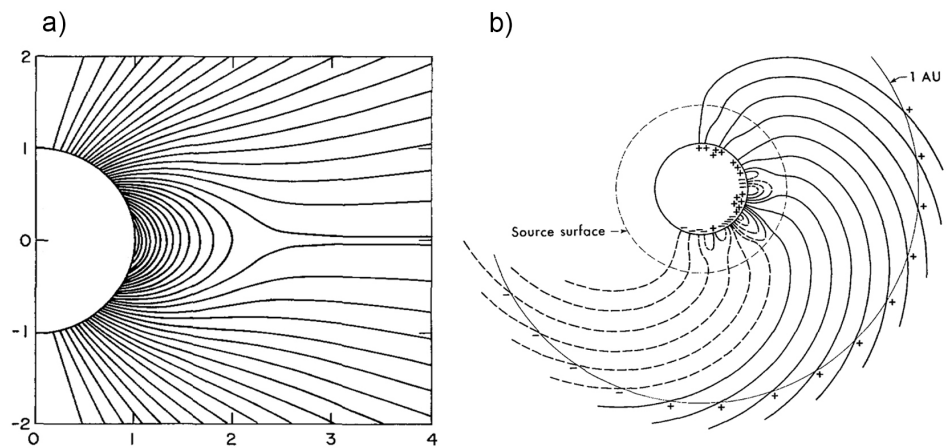


Figure 3.2: The heliospheric magnetic field. a) configuration of the heliospheric current sheet, adapted from Pneuman and Kopp (1971), b) the Parker spiral, adapted from Schatten *et al.* (1969)

lines in the solar wind to describe a spiral, Figure 3.2a. When the solar wind reaches the Earth the magnetic field is oriented at an approximately 45 degree angle from the radial direction, with an average magnetic field of approximately 5 nT (Hultqvist *et al.*, 1999). Due to variations in the solar activity and orientation of the magnetic solar field the current sheet flaps up and down, causing the Earth to alternately be located on either sides of the current sheet. Therefore, the Earth experiences different orientation of the solar wind magnetic field in the two regions. The influence of the orientation of the solar wind magnetic field on the energy transport in the magnetosphere will be discussed in Section 3.5.

3.2 The Magnetosphere

The Earth's magnetic field is generated by the combined effects of convection and rotation of the magma in the Earth's outer core. Close to the Earth the magnetic field can be approximated by a dipole field with a dipole moment of $8 \cdot 10^{15} \text{ T/m}^3$ and with a dipole axis which is tilted approximately 11 degrees from the Earth's rotational axis (Kivelson and Russell, 1995). In the equatorial plane, this corresponds to a surface magnetic field of $30 \mu\text{T}$. The magnetosphere is the region of space which is enclosed by the Earth's magnetic field. The magnetosphere contains a mixture of plasma originating in the solar wind and plasma produced by solar radiation ionizing atmospheric species. The main constituents of the plasma are hydrogen and helium from the solar wind, and oxygen from the ionosphere.

The plasmasphere is a region of closed magnetic field lines containing a cold (10^4 K) and dense ($> 100 \text{ cm}^{-3}$) plasma which forms a torus in the equatorial plane of the Earth, between 3-6 R_E (Hultqvist *et al.*, 1999). The plasmasphere corotates with the Earth and can in many ways be considered an extension of the atmosphere and ionosphere. Despite its relatively small volume, the plasmasphere accounts for a majority of the mass in the Earth's magnetosphere.

Two notable features of the inner magnetosphere are the ring current and the radiation belts. Both consist of particles that due to magnetic mirroring become trapped between the two mirror points on either hemisphere, see Section 2.1. Due to the gradient drift the trapped particles experience a drift motion in the equatorial plane, see Section 2.1. Since curvature drift causes charge separation, this motion sets up an equatorial current going from east to west.

The main difference between the ring current and the radiation belts are the energy of the trapped particles. When talking about the ring current, one typically refers to the low energy, $< 100 \text{ keV}$, particle population which accounts for the majority of the total current (Hultqvist *et al.*, 1999). During quiet conditions the typical ring current density is in the range of $1\text{--}4 \text{ nA/m}^2$, during geomagnetic storms the current density can exceed 7 nA/m^2 (De Michelis *et al.*, 1997). While these may appear to be a small numbers, the increase in the ring current during a substorm corresponds to an energy deposition on the order of 10^{15} J (Knipp *et al.*, 1998; Koskinen and Tanskanen, 2002).

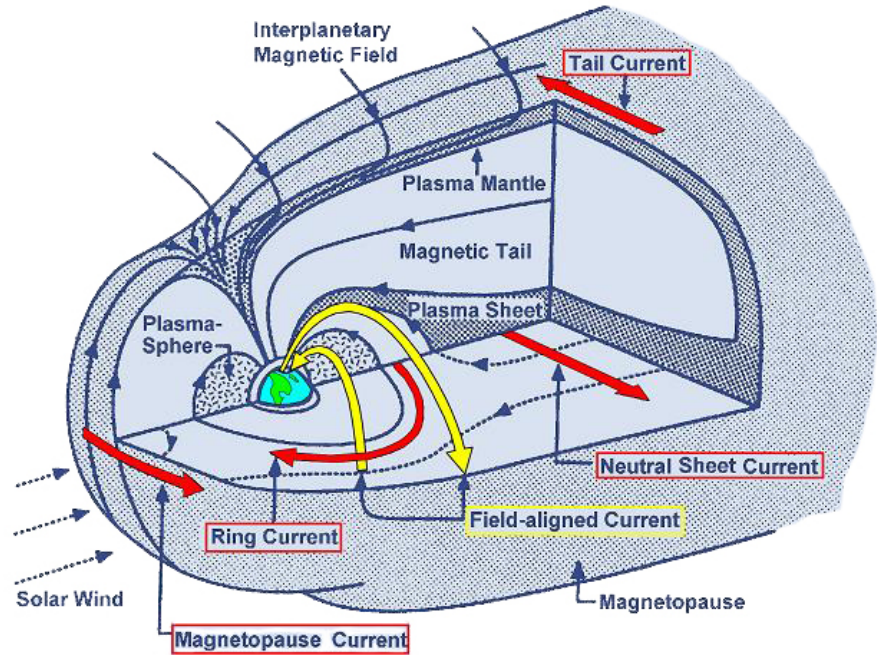


Figure 3.3: Cartoon illustrating the Earth's magnetosphere and associated large scale current systems. Adapted from Kivelson and Russell (1995)

The radiation belts, or Van Allen belts, refer to particles with energies from 100 keV up to hundreds of MeV which populate the inner magnetosphere (Hultqvist *et al.*, 1999). Though they do not significantly contribute to the ring current, they are of great concern since they are sufficiently energetic to penetrate satellites and damage their electronics. The radiation belts consist of an inner belt, between 1.2 and 3 R_E containing both electrons and ions, and an outer belt between 4 and 11 R_E which primarily contains electrons.

The boundary between the solar wind and the magnetosphere is called the magnetopause. At the magnetopause, the dynamic pressure of the solar wind and the magnetic pressure of the geomagnetic field are in equilibrium. For typical solar wind conditions, the magnetopause of the subsolar point is located at approximately 10–12 R_E (Hultqvist *et al.*, 1999). During periods of high solar activity, such as CMEs or flares, the dynamic pressure of the solar wind increases which causes the magnetopause to move inwards.

On the nightside of the Earth, the solar wind sweeps the open field lines anti-

sunward, stretching them into an elongated tail like structure, the so called magnetotail. The magnetotail extends as far as $1000 R_E$ from the Earth and has a diameter of up to $60 R_E$, making it the largest part of the magnetosphere in terms of volume (Hultqvist *et al.*, 1999).

In principle, the magnetotail can be divided in to two main regions, the tail lobes and the plasma sheet. The two tail lobes, which originate in the polar caps, contain open magnetic field lines. That is, field lines which are not connected to the opposite hemisphere of the Earth, and instead close at an extremely large distance from the Earth in the solar wind. Near the Earth, the tail lobes have an extremely tenuous plasma with a density on the order of 0.01 cm^{-3} , but with a significant magnetic field on the order of 20 nT (Kivelson and Russell, 1995). In the tail lobes, the ratio between the magnetic pressure and thermal pressure, β , is $\sim 3 \cdot 10^{-3}$

The plasma sheet is located near the center of the magnetotail. As can be seen in Figure 3.3, the elongated shape causes the magnetic field lines of opposite direction, earthward/anti-earthward on the northern/southern hemisphere, to come in close proximity. This magnetic topology causes a thin current sheet to form, allowing for a transition between the two regions of opposing magnetic fields. This current sheet is often called the cross-tail current, since it goes across the tail from the dawn side to the dusk side, or the neutral sheet as it creates a sheet with a neutral magnetic field. In contrast to the tail lobes, the plasma sheet has a weaker magnetic field, 10 nT , and a higher plasma density, on the order of 0.3 cm^{-3} , with $\beta \sim 6$.

3.3 The Ionosphere

The ionosphere is the upper part of the Earth's atmosphere, extending from 60 to 1000 km . It can be seen as a transition region between the neutral lower atmosphere and the fully ionized magnetosphere. The ionosphere is created through ionization of the neutral atmosphere, either through photoionization by solar light or through ionization by energetic particles. Unlike the magnetosphere, which mostly consists of hydrogen and helium, the ionosphere contains both heavier elements and molecular gases. Combined with the energy input of the sun, this gives rise to several important chemical processes which can modify the composition of the ionosphere.

The ionosphere is gravitationally bound and the relative content of the ion species is strongly affected by the difference in the scale height of their neutral counterpart. As can be seen in Figure 3.4, Hydrogen and Helium, which are only weakly gravitationally bound, dominate at high altitudes, followed by ionized and atomic oxygen at lower altitudes, with molecular nitrogen and molecular oxygen at the lowest altitudes. The dominating charge exchange process in the ionosphere, $\text{H} + \text{O}^+ \leftrightarrow \text{H}^+ + \text{O}$, maintains approximately the same mixing ratio between the two ion species as the neutrals (Hultqvist *et al.*, 1999). Variations in the thermospheric temperature, both from the 11-year solar cycle and geomagnetic disturbances, can change the scale height of oxygen by a factor four, causing the iono-

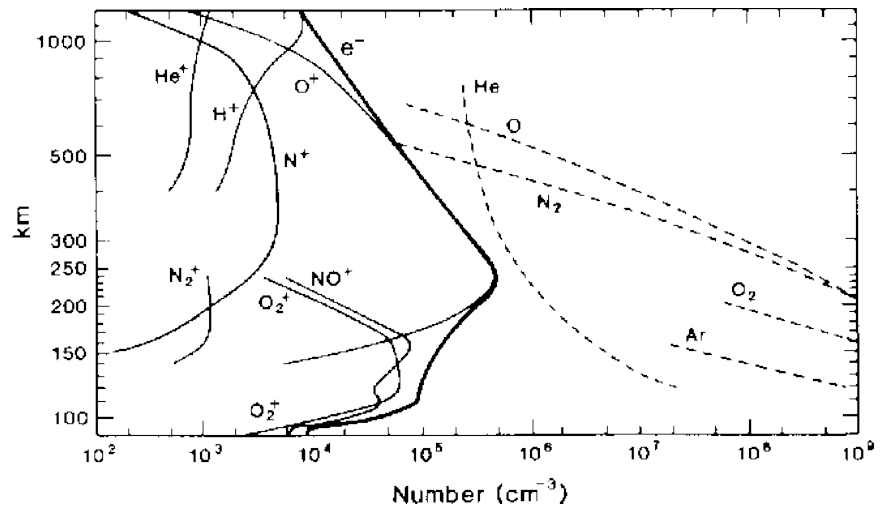


Figure 3.4: Ionospheric ion and neutral composition. From Johnson (1969)

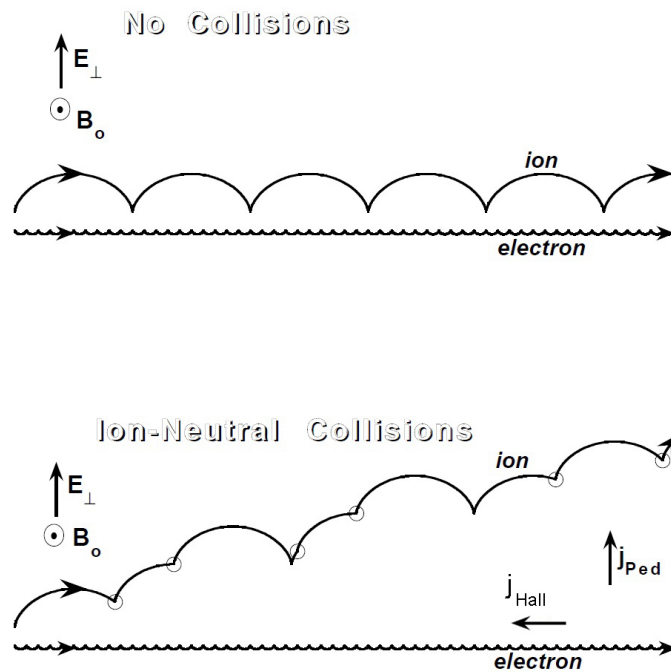


Figure 3.5: Generation of Pedersen and Hall currents. Adapted from Paschmann *et al.* (2003)

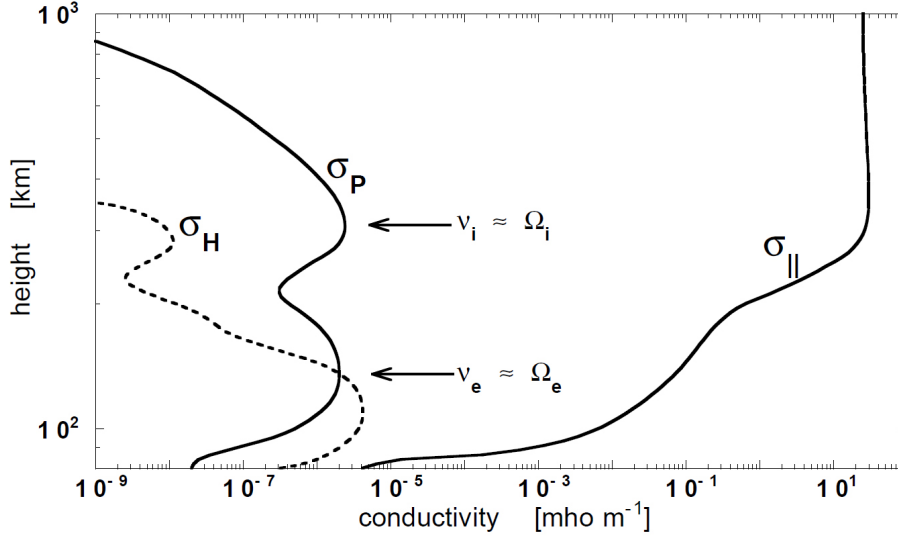


Figure 3.6: Pedersen and Hall currents as a function of altitude. From Paschmann *et al.* (2003)

spheric density of oxygen ions to vary by several orders of magnitude (Hultqvist *et al.*, 1999). During geomagnetic disturbances the ionosphere provides a significant source of oxygen ions to the magnetosphere.

The ionosphere is often divided into several regions, or layers, based on the occurrence of peaks in the electron density. The number of layers and their location varies depending on if the ionosphere is sunlit or not. The nightside ionosphere has two distinct layers, coinciding with peaks in the electron density, the E-layer which is located between 90 to 150 km and the F-layer which extends from 150 km to more than 500 km. The high electron density makes the ionosphere a good conductor which plays an important role in supporting the perpendicular currents of the auroral current systems. The perpendicular conductivity arises from disruptions in the $\mathbf{E} \times \mathbf{B}$ drift, caused by ion-neutral collisions. As can be seen in Figure 3.5, each time the gyro motion is disrupted, the gyro center of the ion shifts in the direction of the electric field. This gives rise to the Pedersen current in the direction of the perpendicular electric field. The collision decreases the average drift velocity of the ions, while the drift velocity of the electrons remain unchanged, this gives rise to the Hall current which is perpendicular to both the magnetic and the electric field. The resulting Pedersen conductivity can be expressed as,

$$\sigma_P = ne^2 \left(\frac{\nu_i}{m_i(\nu_i^2 + \omega_{ci}^2)} + \frac{\nu_e}{m_e(\nu_e^2 + \omega_{ce}^2)} \right). \quad (3.1)$$

where ν_i is the collision frequency of the ions, ν_e is the collision frequency of the electrons, ω_{ci} the ion gyro frequency and ω_{ce} the electron gyro frequency. Similarly the Hall conductivity can be expressed as,

$$\sigma_H = ne^2 \left(\frac{\omega_{ci}}{m_i(\nu_i^2 + \omega_{ci}^2)} + \frac{\omega_{ce}}{m_e(\nu_e^2 + \omega_{ce}^2)} \right). \quad (3.2)$$

As can be seen from Equations 3.1 and 3.2 the Pedersen current scales with the collision frequency while the Hall current scales with the ion gyro frequency. This causes the two conductivities to have different altitude profiles. As can be seen in Figure 3.6, the Hall current dominates at low altitudes. The Pedersen current exhibits two peaks at higher altitudes, one corresponding to the height where the electron collision frequency is equal to the electron gyro frequency and one where the ion collision frequency is equal to the ion gyro frequency.

3.4 Auroral current system

The quiet auroral oval is located on the boundary between open and closed field lines. The oval arises from the occurrence of field aligned currents closing in the ionosphere. The field aligned currents are divided into the poleward, Region 1 current, and the equatorward, Region 2 current. The Region 1 currents arise from the interaction between the solar wind and the flanks of the magnetosphere and the Region 2 currents map to the partial ring current (Kivelson and Russell, 1995). As can be seen in Figure 3.7a, Region 1 carries upward current on the dusk side and downward current on the dawn side, while Region 2 carries downward current on the dusk side and upward current on the dawn side. During quiet conditions, the current closure is both through Hall currents in eastward and westward electrojets (Figure 3.7b) and through Pedersen currents oriented in the north-south direction (Figure 3.7c).

3.5 The substorm cycle

One of the important mechanisms for transferring energy and plasma, from the solar wind to the magnetosphere, is magnetic reconnection. Magnetic reconnection is a violation of ideal MHD and can change the topology of the magnetic field. Reconnection at the dayside magnetopause and in the magnetotail provides the energy which drives the auroral substorms. Magnetic reconnection can occur when there is a large enough shear between two magnetic fields, at the dayside magnetopause, where the geomagnetic field is northward, this equates to a southward component in the solar wind magnetic field. For a northward component in the solar wind magnetic field reconnection will typically occur at higher latitudes on tail lobe magnetic field lines.

As can be seen in Figure 3.8, reconnection causes the open field lines of the solar wind to merge with the originally closed field lines of the geomagnetic field. This

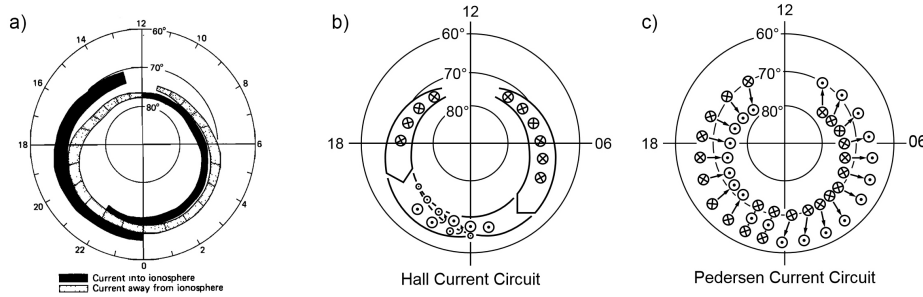


Figure 3.7: The current systems of the auroral oval. a) the region 1 and region 2 field aligned currents, adapted from Iijima and Potemra (1978), b) the Hall current auroral electro jets, c) the Pedersen currents, adapted from Baumjohann (1997)

transforms the closed geomagnetic field lines into open field lines which convect anti-sunward with the solar wind. This increases the number of open field lines, causing an accumulation of magnetic energy in the two tail lobes. As a consequence, the polar cap grows in size and the auroral oval moves equatorward, corresponding to the so called growth phase of the substorm (McPherron, 1970).

Whereas dayside reconnection stores magnetic flux and energy in the tail lobes, reconnection in the magnetotail releases the stored energy. In the central plasma sheet, the shear between the earthward magnetic field of the north tail lobe and anti-earthward in the south tail lobe, causes the stretched field lines to reconnect. Tailward of the reconnection site, the recently closed field lines are ejected away from the Earth as a plasmoid. Earthward of the reconnection site, the recently closed field lines are no longer subject to the solar wind induced convection and snap back towards the Earth, returning them to a more dipolar configuration. This reduces the number of open field lines and returns the magnetosphere to a more closed configuration. As a result, the polar cap shrinks and the auroral oval moves poleward. As illustrated in Figure 3.9, the fast earthward plasma flows associated with the depolarization disrupts the cross tail current, causing it to be diverted, along the magnetic field lines into the ionosphere. This current intensification is known as the substorm current wedge.

In contrast to the current system of the quiet time auroral oval, the closure of the substorm current wedge is a much more localized phenomenon. The current closure in the ionosphere is primarily through east-west Hall currents known as the auroral electrojet. On average, the auroral electrojet extends between 22–02 hours magnetic local time (MLT) (Kepko *et al.*, 2014). This causes an initial brightening of the auroral oval near local midnight and a poleward expansion of the auroral oval. This is known as the expansion phase of the substorm and is associated with development of several types of dynamic auroral morphologies and breakup of continuous arcs into patches of aurora (Akasofu, 1964).

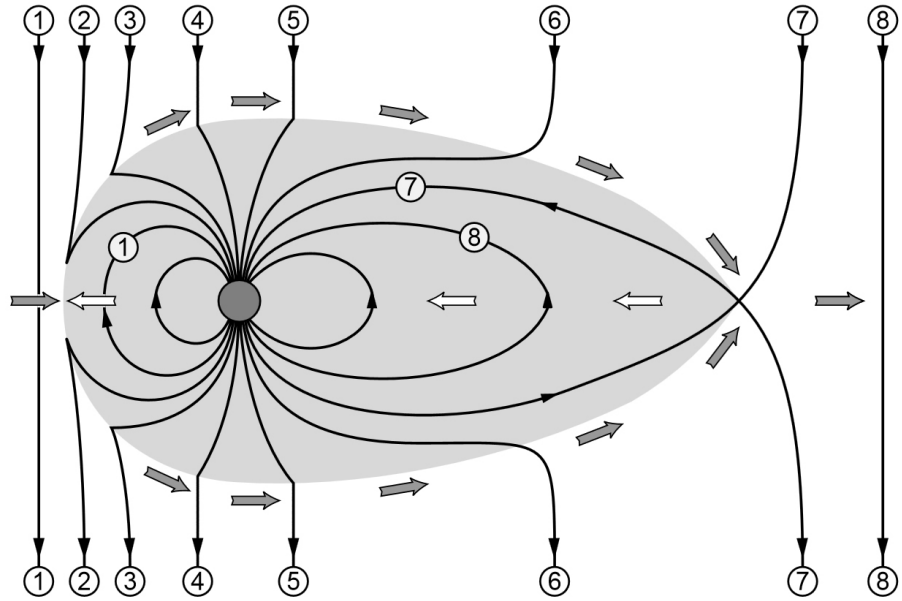


Figure 3.8: Cartoon illustrating the Dungey cycle. Adapted from Baumjohann (1997)

3.6 The Auroral Density Cavity

The first observations of the Auroral Density Cavity (ADC) were made by early satellite missions studying the Earth's magnetosphere. Data from the low-frequency radio experiment onboard the satellite OGO1 showed that the Earth exhibited intense radio emissions starting at 20 kHz and reaching up to the instrument limit of 100 kHz (Dunckel *et al.*, 1970). These emissions had not been observed previously since they were shielded out by the ionosphere. Subsequent data from the satellites Imp 6 and Imp 8 showed that the emissions, which had total power of up to 10^8 W, originated from the low altitude auroral region and would typically cover a frequency range of 50–500 kHz (Gurnett, 1974).

These intense radio emissions were subsequently named Auroral Kilometric Radiation (AKR), after their characteristic wavelength. The ISIS 1 mission revealed that AKR generation occurred in regions with depleted electron density and was associated with precipitation of inverted-V electrons (Benson and Calvert, 1979; Benson *et al.*, 1980). This observation was in agreement with the electron-cyclotron maser theory of AKR generation, where an inverted-V population, typically in the keV range, provides the free energy (Wu and Lee, 1979; Melrose *et al.*, 1982).

This region of low electron density was subsequently named the auroral plasma

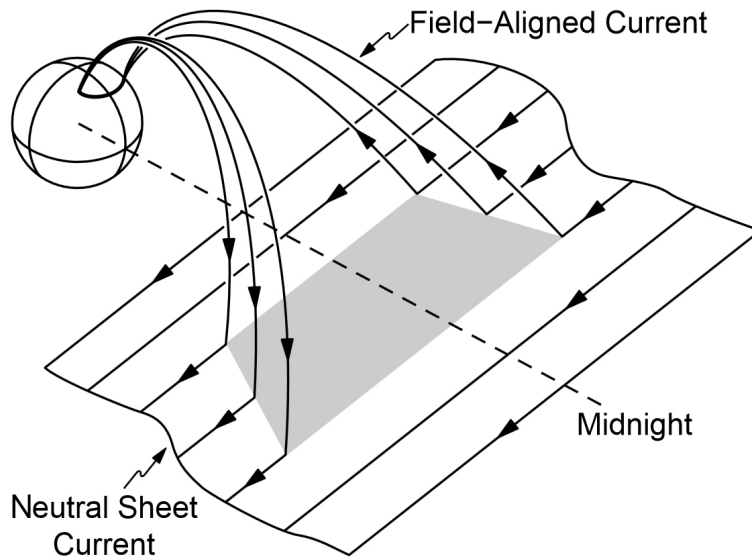


Figure 3.9: Cartoon illustrating the closure of the substorm current wedge through the ionosphere, adapted from Baumjohann (1997)

cavity or the auroral density cavity. An early statistical study, using data from the Hawkeye satellite showed, that auroral density cavities with an electron density $< 1 \text{ cm}^{-3}$ was typically located between $1.8\text{--}3 R_E$ and at an invariant latitude of 70 ± 3 degrees. The density cavity exhibited a distinct poleward boundary which separated it from the polar cap while the equatorward boundary was found to be indistinguishable from the plasmopause (Calvert, 1981).

Data from the satellite Dynamics Explorer 1 indicated that the ADC is a common phenomenon in the auroral region. The cavities were observed between 70 ± 5 degrees invariant latitude, from magnetic local times in the pre-dusk hours until early morning and for geocentric altitudes up to $4.6 R_E$. Inside the density cavities, the minimum electron density was often lower than 0.3 cm^{-3} and only rarely higher than 3 cm^{-3} (Persoon *et al.*, 1988).

A statistical study, using data from the Polar satellite, showed that density cavities were common between $68\text{--}74$ degrees invariant latitude, in the geocentric altitude range of $2\text{--}4 R_E$. In addition, a second population of high-altitude density cavities, located above $4 R_E$, were found to be correlated with $k_p\text{-index} > 2$, corresponding to substorm conditions (Janhunen *et al.*, 2002).

Our current understanding is that the auroral density cavity consists of a mixture of cold, dense plasma ($T_e < 1 \text{ eV}$, $n_e \sim 10^1\text{--}10^5 \text{ cm}^{-3}$) of ionospheric origin and a tenuous cavity plasma consisting of cold, ionospheric ions and hot plasma

sheet electrons ($T_e \sim 500$ eV, $n_e \sim 1$ cm⁻³) (Ergun *et al.*, 2004; Hull *et al.*, 2003). Satellite observations suggest that the density cavity has little cold electrons, accounting for less than 20 % of the total electron content (McFadden *et al.*, 1999; Mozer and Hull, 2001; Paschmann *et al.*, 2003). In addition, the hot plasma sheet electrons have been known to exhibit a significant high energy tail, which deviates from the classical Maxwellian distribution (Olsson and Janhunen, 1998). Data from the Polar satellites electron spectrograph, Hydra, have shown that Kappa distribution offers a better fit to the observed distributions twice as often as Maxwellian distributions (Kletzing *et al.*, 2003).

3.7 The Auroral Acceleration Region

The auroral acceleration region arises from the requirement of current closure in the auroral current systems. Due to their high mobility, the majority of the current is carried by electrons rather than ions. In the downward current region the current, carried by upward flowing electrons, can flow more or less unimpeded. However, in the upward current region magnetic mirroring (see Section 2.1) reduces the number of electrons that are able reach the ionosphere, thus limiting the current. For small loss cone angles, the fraction of the electron distribution which is inside the loss cone can be described by,

$$\tilde{f} = \frac{\pi\theta_{lc}^2}{2\pi} \sim \frac{B_{eq}}{B_{ion}}, \quad (3.3)$$

where B_{eq} is the magnetic field of the flux tube at the equator and B_{ion} is the magnetic field of the flux tube at the ionospheric foot point (Paschmann *et al.*, 2003). In order to close the current, the parallel velocity of the electrons must be increased, pushing more electrons into the loss cone. In principle, parallel acceleration can be divided into two types of mechanism, quasi-static acceleration and Alfvénic acceleration. While the two types of acceleration are often seen in different regions, there have been observations of mixed acceleration and regions of quasi-static acceleration forming out of predominately Alfvénic regions (Hull *et al.*, 2010; Marklund *et al.*, 2011; Li *et al.*, 2013).

The idea that the auroral electrons were accelerated by quasi-static parallel electric fields was first proposed by Hannes Alfvén in 1955. Quasi-static acceleration refers to acceleration processes in which the parallel electric fields change little over the time it takes for an electron to pass through the acceleration region. Quasi-static acceleration is associated with a narrow energy distribution, with a the peak flux at energies corresponding to the parallel potential drop above the satellite. Due to the magnetic mirror forces, the electrons have a nearly isotropic pitch angle distribution with the exception of a clear loss cone in the upward direction. The parallel potential drop required to carry the field aligned current, assuming an

isotropic Maxwellian electron distribution can be described by the Knight relation,

$$j_{\parallel,ion} = en \left(\frac{k_B T_e}{2\pi m_e} \right)^{1/2} \left\{ (R_M - 1) \exp \left[-\frac{e\Delta\Phi_{\parallel}}{k_B T_e (R_M - 1)} \right] \right\}, \quad (3.4)$$

where $\Delta\Phi_{\parallel}$ is the parallel electric potential drop and R_M is the ratio between the ionospheric magnetic field and the magnetic field at the top of the acceleration region B_{ion}/B_{top} (Knight, 1973). Under the condition that, $1 \ll e\Delta\Phi_{\parallel}/k_B T_e \ll R_M$, the Knight relation can be linearized as,

$$j_{\parallel,ion} = \frac{e^2 n_e}{\sqrt{2\pi m_e k_B T_e}} \Delta\Phi_{\parallel}. \quad (3.5)$$

The Knight relation has been tested experimentally, indicating a good overall agreement between observed currents and parallel potential drops (Lu *et al.*, 1991; Haerendel *et al.*, 1994). Similarly Knight's relation has been modified to encompass other electron distributions than Maxwellians (Janhunen and Olsson, 1998; Dors and Kletzing, 1999).

The quasi-static parallel electric field is often difficult to measure directly but can be inferred from measurements of the perpendicular electric field. Strong converging perpendicular electric fields are often observed at high altitudes but which do not map to the ionosphere (Mozer *et al.*, 1977). This implies that a region of upward parallel electric field must exist in order to close the converging perpendicular electric fields. There are several different proposed mechanisms generating the quasi-static parallel electric fields such as: double layers (Alfvén, 1955), anomalous resistivity (Hudson and Mozer, 1978) and parallel electric fields supported by the magnetic mirror force (Knight, 1973).

Several different types of double layers have been studied, such as strong double layers (Block, 1972) and weak double layers (Temerin *et al.*, 1982). There have been several numerical simulations of double layers located at the lower edge of the auroral acceleration region (Ergun *et al.*, 2000, 2002b). The simulations have shown that such double layers are stable in time and can form out of a large number of initial particle populations (Main *et al.*, 2006, 2010).

Alfvén waves with small transverse wavelength, which carry a parallel electric field, can result in Alfvénic parallel acceleration (Song and Lysak, 2001). The electron signature of Alfvénic acceleration is characterized by counterstreaming electrons, field aligned and anti-field aligned, with a broad energy distribution in some cases reaching above 10 keV (Paschmann *et al.*, 2003). Alfvénic auroral arcs can be very narrow, less than 100 m, and exhibit an optical brightness in excess of 100 kR (Chaston *et al.*, 2006). Alfvénic acceleration is often seen near the polar cap boundary but can also be observed within quasi-static arc systems (Marklund *et al.*, 2012). In contrast to quasi-static arcs, Alfvénic arcs are not directly associated with pronounced density cavities. The FAST satellite has observed low-altitude, ionospheric density cavities, which are believed to be generated by Alfvénic acceleration (Chaston *et al.*, 2006). In contrast, observations from the Cluster satellites

have shown that Alfvénic activity may prevent the formation of a density cavity (Marklund *et al.*, 2011, 2012; Alm *et al.*, 2013).

One tool for distinguishing between quasi-static and Alfvénic acceleration is looking at the ratio between the perpendicular electric field and the perturbation magnetic field. For a quasi-static structure this corresponds to,

$$\frac{E_{\perp}}{\Delta B} = \pm \frac{1}{\mu_0 \Sigma_P}, \quad (3.6)$$

where E_{\perp} is the perpendicular electric field, ΔB is the perturbation magnetic field, and Σ_P is the Pedersen conductance. For an Alfvénic structure the ratio can be expressed as,

$$\frac{E_{\perp}}{\Delta B} = \pm \frac{1}{\mu_0 \Sigma_A} = \pm V_A, \quad (3.7)$$

where Σ_A is the Alfvénic conductance and V_A the Alfvén speed. Typically, Σ_A is much smaller than 0.1 S, while Σ_P is approximately 10 S (Paschmann *et al.*, 2003). Therefore the $E_{\perp}/\Delta B$ ratio is generally much larger for Alfvén waves than for quasi-static structures. In addition, the Alfvén speed can be expressed as,

$$V_A = \frac{B}{\sqrt{\mu_0 n_i m_i}} \quad (3.8)$$

where n_i is the number density of the ions and m_i is the average ion mass. Note that the electrons can be ignored due to their low mass. This allows us to estimate the degree of Alfvénic acceleration using the ratio, $(E_{\perp}/\Delta B)/V_A$. Ideally, a purely Alfvénic structure should have a ratio which does not significantly differ from 1, though ratios higher than 1 are possible. If the ratio is significantly lower than 1 this indicates that the acceleration is predominately quasi-static.

Chapter 4

The Cluster Mission

The Cluster mission has had its share of both disaster and success. The original Cluster satellites were launched in 1996, on what was supposed to be the maiden voyage of the European Space Agency's Ariane 5 rocket. The flight lasted 39 seconds, until a software error causes the rocket to veer off course and begin to disintegrate, which caused the ground crew to self-destruct the launch vehicle along with its payload. The aftermath was that four copies of the original Cluster satellites were built and launched as part of the Cluster II or Phoenix mission (Escoubet *et al.*, 2012), here on after referred to as "Cluster".

Cluster consists of a constellation of four identical satellites which were launched from the Baikonur Cosmodrome in July and August 2000 by two Soyuz-Fregat rockets. Their mission is to study a wide variety of plasma physical phenomena in the Earth's magnetosphere. Originally, Cluster's polar orbit had a perigee of $4.0 R_E$, an apogee of $19.2 R_E$ and an inclination of 89.6 degrees, resulting in an orbital period of approximately 57 hours. As a consequence of the Earth's orbit around the Sun, the plane of the orbit shifts over the year allowing the constellation to cover the solar wind and magnetopause during the northern hemisphere winter, as well as the magnetotail during the northern hemisphere summer. Over the years, the orbit has changed significantly. The perigee has exhibited a gradual decrease, allowing Cluster to observe new regions of interest. In 2009, the perigee of the satellites had decreased to approximately $2 R_E$ and the argument of perigee had changed allowing for direct observations of the central parts of the auroral acceleration region. In addition, several orbital maneuvers have been performed to raise the perigee. The annual cycle and long term evolution of the Cluster constellations orbit is illustrated in Figure 4.1.

The mission was originally planned to last two years, but is currently entering its 16th year. This has allowed Cluster to observe over a full solar cycle and its influence of the Earth's magnetosphere. Though some of the instruments have suffered malfunctions all four satellites are still largely operational.

Combining observations from four spacecraft allows for detailed data analysis

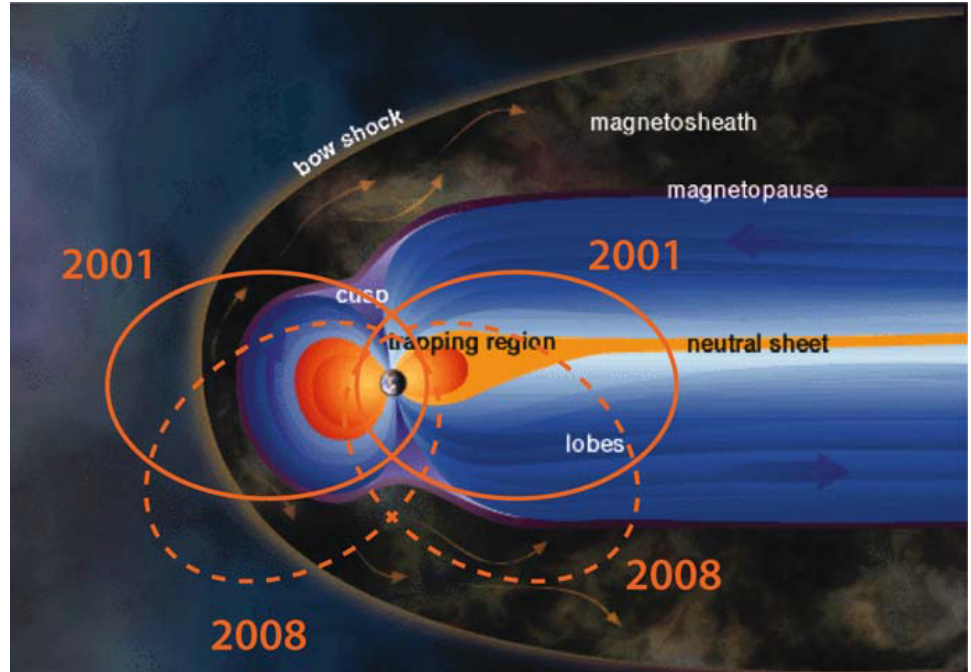


Figure 4.1: Orbital evolution of the Cluster constellation. From Laakso *et al.* (2010)

without relying on many of the assumptions and approximations required for single spacecraft observations. We can, for the first time, separate between spatial and temporal variation, which allows Cluster to provide a truly three dimensional picture of many transient phenomena such as magnetic reconnection.

The combination of capable instruments, multi-spacecraft measurements and long life time has contributed to make Cluster a highly successful and productive mission. As of July 2015, 2217 peer-review articles based on Cluster data have been published.

4.1 Cluster Ion Spectrometry

The Cluster satellites analyze the plasma ion composition and energy distribution using the instrument Cluster Ion Spectrometry (CIS) (Rème *et al.*, 1997). The instrument provides three dimensional ion spectrometry and can determine the composition through charge/mass separation of the ions. CIS consists of two sub-instruments: COmposition and DIstribution Function (CODIF) and Hot Ion Analyzer (HIA). Each sub-instrument has a low and high sensitivity sensor in order to accommodate a particle flux range of approximately seven orders of magnitude

Table 4.1: Summary of the operational history of CIS instruments. From Dandouras and Barthe (2014).

	C1	C2	C3	C4	
CODIF	Operations until 25 Oct. 2004	Not operational	operational	One deficient MCP quadrant, until switch-off on 11 Nov. 2009	Normal operations
HIA	Operational 1 hour/orbit of November 2012.	Not operational	operational	Normal operations until 11 Nov. 2009	Not operational

particle without risking sensor saturation. The two sensors each covers a 180 degree arc which over the course of one satellite spin period, 4 s, generates a full 4π solid angle coverage (Rème *et al.*, 1997).

CODIF utilizes a combination of ion charge/energy selection through a toroidal electrostatic analyzer and a time-of-flight analyzer. This allows CODIF to separate between different ion species for a specific energy/charge ratio. CODIF has an energy/charge range of 25 eV/e - 40000 keV/e and a mass range of 1 - 32 amu. CODIF completes a full energy sweep 32 times per spin period, approximately every 125 ms. The sensors have a 180 degree field of view, divided into 8 polar sectors, resulting in an angular resolution of 22.5 degrees (Dandouras and Barthe, 2014).

HIA utilizes a quadrispherical analyzer with electrostatic deflection to achieve a higher energy/charge resolution than that of CODIF, while sacrificing the ability to separate between different ion species. HIA is equipped with a total of 62 energy channels, giving it an energy/charge range of 5 eV/e - 32 keV/e. During nominal operations a full energy sweep is conducted every 62.5 ms (Rème *et al.*, 1997). In order to comply with the telemetry allocation and mode of operations, different binning schemes are used so that energy 32 channels are available at any give time. The HIA sensors have a combined 180 degree angular coverage, which is divided into 16 polar zones resulting in an angular resolution of 11.25 degrees (Dandouras and Barthe, 2014).

Since launch, several of the CIS instruments have suffered malfunctions, most notably C2 which has not delivered any data since launch. As of November 2012, only the CODIF sub-instrument of satellite C4 remains operational (Dandouras and Barthe, 2014). The operational history of CIS is summarized in Table 4.1.

4.2 Electric Field and Waves

The Electric Field and Wave (EFW) instrument consist of four Langmuir probes located at the end of 44 m spin plane wire booms. The electric field is determined from the potential difference between two opposite Langmuir probes. This allows EFW to measure the electric field in the spin plane with a sampling frequency up to 25 Hz in normal mode and 450 Hz in burst mode (Gustafsson *et al.*, 1997).

The raw electric field data is in the rotating satellite frame and is despun into an inertial coordinate system. The despun electric field data will contain electric fields introduced by the motion of the satellite across the magnetic field, $\mathbf{E} = -\mathbf{v} \times \mathbf{B}$, which must be subtracted. For the standard data sets, the Inverted Spin Reference (ISR2) coordinate system is used. In the ISR2 coordinate system, the x-axis points as near sunward as possible, the y-axis lies in the spin plane, perpendicular to the x-axis, and the z-axis lies along the negative of the spin axis. The unprocessed electric field data is also used by other Cluster experiments focusing on high frequency phenomena.

Due to probe failures since launch, not all of the probe pairs remain operational. This has led to a gradual loss in the availability of high resolution electric field data. However, the standard spin resolution, 4 s, data is as of 2015 still available on all four Cluster satellites (Lindqvist *et al.*, 2014).

Since EFW is not equipped with spin axis double probes, the electric field along the spin axis is not measured directly. Instead, the third electric field component is calculated assuming that $\mathbf{E} \cdot \mathbf{B} = 0$. As a result, the three dimensional data set will, by definition, not contain any electric field component parallel to the geomagnetic field. This can be a complication when studying auroral physics, where parallel electric fields are an important phenomenon.

Spacecraft potential

The spacecraft potential is governed by the current balance between the photoelectron current leaving the spacecraft and particle collection through collisions between the satellite and the plasma. The photoelectron current is dependent on the solar flux and characteristics of the illuminated surface. The current contribution from the surrounding plasma is in turn strongly affected by the plasma density and temperature. As long as the satellite remains illuminated, the photo electron current changes over much larger time scale, than the plasma electron density. This allows the spacecraft potential to serve as proxy measurement for electron density variations occurring over short to intermediate time scales.

The spacecraft potential is defined as the potential difference between the spacecraft and the surrounding plasma. The spacecraft potential found in the Cluster data sets is defined as the potential difference between the plasma and the spacecraft, $\Delta P_{SC} = P_{plasma} - P_{SC}$. Therefore, the spacecraft potential will generally assume negative values in the Earth's magnetosphere.

Table 4.2: Summary of FGM operating ranges and resolutions. From Carr *et al.* (2014).

Mode Number	Range [nT]	Resolution [nT]
2	-64 to +63.97	$7.8 \cdot 10^{-3}$
3	-256 to +255.87	$3.1 \cdot 10^{-3}$
4	-1,024 to +1,023.5	0.125
5	-4,096 to +4,094	0.5
6	-16,385 to +16,376	2
7	-65,536 to +65,536	8

Spacecraft potential is available as a separate data set from the Cluster Science Archive. The time resolution is the same as of the electric field measurements, typically the 4 s spin resolution (Lindqvist *et al.*, 2014).

4.3 Fluxgate Magnetometer

Cluster measures magnetic fields using two triaxial FluxGate Magnetometers (FGM), one located at the end of a 5.2 m axial boom and one 1.5 from the tip of the boom (Balogh *et al.*, 1997). The raw data is acquired at a rate of 201.75 Hz, though due to bandwidth limitation the full time resolution is not available for download. The data acquisition frequency is limited to 22 Hz for normal mode data and 67 Hz for burst mode data. The standard data set has a data acquisition frequency of 5 Hz. Due to the large variations in the geomagnetic field strength throughout the satellite's orbit, FGM operates in six different modes, with varying range and resolution. These modes are outlined in Table 4.2.

As of 2014 the FGM instruments were operational on all four Cluster satellites. FGM has had very high data availability and has operated continuously since launch. Major data gaps are typically associated with mission-related issues rather than instrument malfunctions.

The magnetic field data can be used to estimate field aligned currents, a phenomenon which is typical for the auroral region. This process is outlined in Section 5.4. In addition, the FGM instrument is vital in providing reference data for several other instruments such as the electron and ion spectrometers, the electric fields and waves instrument and the electron drift instrument.

4.4 Plasma Electron And Current Experiment

The four Cluster satellites are each equipped with a top hat electrostatic electron analyzer, Plasma and Electron And Current Experiment (PEACE) (Johnstone *et al.*, 1997). The PEACE instrument consists of two different sensors, the Low Energy Electron Analyzer (LEEA) and the High Energy Electron Analyzer (HEEA). The two sensors are designed for optimal coverage of their respective energy range. At

Table 4.3: Summary of the operational history of PEACE instruments. From Fazakerley (2014).

	C1	C2	C3	C4
LEEA	Normal operations	Anode 2 not operational from 22 Aug. 2005	Normal operations	Normal operations
HEEA	Normal operations	Normal operations	Anode 1 not operational from 15 May. 2005	Normal operations

lower energies the particle flux is typically significantly larger than at the higher energies. In order to avoid sensor saturation LEEA has a smaller geometric factor than HEEA. The combined energy coverage of LEEA and HEEA is 0.6 eV - 26,460 eV (Fazakerley, 2014).

The two sensors are divided into 12 polar anodes, each covering a 15 degree sector, from anti-spin aligned to spin aligned. The two sensor are located on opposite sides of the spacecraft and over the course of one spin period both sensors has full 4π solid angle coverage.

The instrument has a data link with FGM which allows the on-board data processing to produce pitch angle resolved data from the full three dimensional distributions. In addition, electron moments are calculated using the three dimensional particle data which gives information on electron temperature, electron density and bulk velocity. The standard time resolution of the PEACE data sets are one spin period, 4 s, but some data set can also be available in half-spin and sub-spin resolution.

In order to avoid radiation damage to the instruments' micro channel plates and electronics, the instruments are generally switched off at magnetic shells lower than L=6. As of 2014 the PEACE instruments are operational on all four Cluster satellites, though some of the instruments have suffered partial failures. One of the anodes on C2 and on C3 are no longer operational. This affects the accuracy of the electron moment calculations on C2 and C3 and will lead to incomplete pitch angle data for certain magnetic field configuration (Fazakerley, 2014). For more details on the operational history of PEACE, see Table 4.3

4.5 Waves of High frequency and Sounder for Probing of Electron density by Relaxation

The experiment Waves of High frequency and Sounder for Probing of Electron density by Relaxation (WHISPER) serves two purposes. The first is to continuously monitor natural plasma emissions in the 2–80 kHz range. The second purpose is to determine the local electron density from the electron plasma frequency (Décréau *et al.*, 1997).

WHISPER uses electric field measurements from the double probes of the EFW experiment, which are filtered, digitized and spectrum analyzed by the on-board Fast Fourier Transform (FFT) computer. A complete 0–83 kHz spectral sweep last for 13.33 ms, dividing the spectrum into either 256 or 512 frequency bins.

WHISPER can be operated in two different modes, a passive, natural wave mode and an active sounding mode. The data from the natural wave mode is produced from several successive spectra in order to remove transient features and increase the signal-to-noise ratio. Depending on the telemetry options the resolution of the data product can range from 0.326 s to 3.4 s, with a typical resolution of 2.15 s. In the sounding mode WHISPER transmit millisecond wave trains, which typically cover a frequency range of 976.6 Hz. After a short delay the receivers located in the EFW experiment are switched on and record the returning signal. This process is repeated for a new frequency ranged until the entire 4–82 kHz range has been covered (Trotignon and Vallières, 2014).

The two operation modes are used in tandem with each other. Under normal operations, 3 s of sounding mode is followed by 49 s of natural mode, which results in a combined time resolution of 52 s for a complete measurement cycle.

Electron density from WHISPER

The electron density is determined from the signature of the electron plasma frequency. In the natural wave mode the electron plasma frequency is determined from the cut-off frequency of the natural wave mode. In the sounding mode it can be determined from the signature of resonance at the electron plasma frequency. Since data from both modes are employed, the typical time resolution of the electron density data is 52 s. Since the electron density is determined by the electron plasma frequency, the density range of WHISPER is determined by its frequency range. For the purpose of electron density estimations, the frequency range is 4–82 kHz which corresponds to a density range of 0.2–83 cm⁻³.

The quality of the electron density estimations are given by the contrast quality factor. The contrast refers to how clear the signature of the electron plasma frequency is in the spectrogram. The quality factor is normalized so that 0 corresponds to the data with the lowest quality and 1 corresponds to the best quality available. This allows us to estimate how reliable the electron density estimations are.

Chapter 5

Methodology

5.1 High resolution electron density measurements

As described previously, both WHISPER and EFW can be used to estimate the electron density. While WHISPER can make direct measurements, the 52 s time resolution is often a limiting factor when studying auroral phenomena. Crossing through an auroral arc will often take only a few minutes, which results in very little WHISPER electron density data being available for a single auroral arc. In contrast, the spacecraft potential measurements from EFW are available with high time resolutions, typically 0.2 s. The main drawback of the spacecraft potential is that it does not provide an absolute value of the electron density. By combining the WHISPER and EFW we can create a calibration curve converting the high resolution spacecraft potential measurements into their corresponding electron densities. The relation between the spacecraft potential and electron density is in its fundamental form fairly complex but can for these purposes be approximated by a double exponential,

$$n_e(P_{SC}) = n_1 \cdot \exp(e\Delta P_{SC}/k_B T_1) + n_2 \cdot \exp(e\Delta P_{SC}/k_B T_2), \quad (5.1)$$

where n_e is the electron density, P_{SC} is the spacecraft potential and T_n is the electron temperature of the respective Maxwellian distribution (Scudder *et al.*, 2000; Pedersen *et al.*, 2008). In terms of applying this to Cluster data we can simplify Equation 5.1 as,

$$n_e(P_{SC}) = c_1 \cdot \exp(\Delta P_{SC}/c_2) + c_3 \cdot \exp(\Delta P_{SC}/c_4), \quad (5.2)$$

where c_n are the four calibration coefficients to be determined. There are two main methods for determining the calibration coefficients. If sufficient WHISPER data are available for each of the events in question, the calibration can be performed on a case by case basis. This is the preferred method whenever possible. For cases when sufficient WHISPER data are not available, the calibration can also be conducted on a statistical basis. The properties of the plasma vary in different

regions of the magnetosphere and the solar flux exhibits seasonal changes as well as variations over the solar cycle. These variations affect the stability of the calibration curve. In addition, a sufficient number of data points must be available to produce a sufficiently stable statistical calibration curve. Sensitivity studies have shown that in the auroral region, 105 days is a good compromise between achieving a sufficiently large data set and being able to account for the seasonal variations of the calibration curve (Li *et al.*, 2014).

5.2 Estimating parallel electric fields

As discussed in Section 4.2, the standard EFW data sets do not contain any information on the parallel electric field. It is possible, under some circumstances, to recover some data on the parallel electric field from the EFW two dimensional data sets. However, this process is highly dependent on the orientation of the satellite relative the geomagnetic field and susceptible to computational artifacts.

One method for estimating the parallel electric field is to utilize the electron spectrogram from PEACE and the ion spectrogram from CIS. In the upward current region, the potential drop above the spacecraft can be estimated by the characteristic energy of the precipitating inverted-V electrons and the parallel potential drop below the spacecraft by the characteristic energy of the upward ion beam. The characteristic energy is the total energy flux divided by the total particle flux (Paschmann *et al.*, 2003). In terms of Cluster's electron and ion data sets can be expressed as,

$$\Phi_{\parallel} = W_{char} \equiv \frac{\sum_{i=1}^{imax} W_i \phi_i \Delta W_i}{\sum_{i=1}^{imax} \phi_i \Delta W_i}, \quad (5.3)$$

where W_i is the energy of energy bin i , ϕ_i the differential particle flux of energy bin i and ΔW_i the width of energy bin i . The electron spectrograms will often exhibit a large flux of electrons in the range of a few tens of eV. This is a population of photo electrons which have been re-attracted by the spacecraft potential and thus not representative of the distribution of the surrounding plasma. Due to their high flux they can have a significant impact on the calculation of the characteristic energy, especially for auroral arcs with a low flux of inverted-V electrons. Therefore, it is recommended that the calculation of the characteristic energy should only be performed on energy bins well above the corresponding spacecraft potential.

Alternatively, the parallel potential drop above the satellite can be determined from the local maximum in the phase space density (PSD) of the precipitating electrons, caused by the parallel acceleration. Compared to using the characteristic energy, this method is more labor intensive since it often must be performed by hand. In addition, the resulting parallel potential drops will only assume a discrete number of values, corresponding to the energy bins of the instrument. This reduces

the resolution of the estimated parallel potential drop. The advantage is that this method offers a better physical representation of the parallel potential drop and that the width of the energy bin offers an error estimate.

Alternatively, the parallel potential drop below the spacecraft can be estimated by integrating the perpendicular electric field along the path of the spacecraft and subtracting the ionospheric potential (Mozer and Kletzing, 1998). Electric field data has the advantage of a higher availability compared to CIS-HIA ion spectrograms, which are only available from spacecraft C1 and C3. However, since we cannot separate between temporal and spatial variation in the electric field, the integration along the satellite's path may introduce systematic errors in the estimated parallel potential drop. Furthermore, the process of fitting and subtracting the ionospheric potential can sometimes struggle to describe small scale features seen in the ion spectrograms, though they often result in similar values for the maximum parallel potential drop. It is therefore preferable to use the ion characteristic energy to estimate the parallel potential drop below the spacecraft, when available.

An estimate of the parallel electric field can be achieved by comparing the change in the parallel potential drop, estimated from the electrons or ions, with the vertical motion of the satellite. In a region containing a parallel electric field, the change in the characteristic energy of the electrons and ions should be of equal magnitude but of opposite signs. However, in reality there are several factors which can affect the accuracy of the estimated parallel electric field.

If the total parallel potential drop is not constant between adjacent measurements, either due to gradual closure of equipotential lines below the satellite, or due to small scale potential structures above the satellite, it will cause the characteristic energy of the ions or electrons to change in a way that does not reflect the local parallel electric field. In addition, the limited energy and time resolution of PEACE and CIS can cause random variations in the respective characteristic energy which does not correspond to local parallel electric fields.

An important sanity check is to verify that the predicted parallel electric field is in agreement with the direction of the parallel current and the observed electron and ion populations. For example, if we observe precipitating inverted-V electrons and an upgoing ion beam, estimates of a downward parallel electric field is likely a computational artifact. Keeping these complications in mind, the parallel electric field can be estimated by,

$$E_{||}(t) = \begin{cases} \frac{\min(|\Delta\Phi_{||,a}(t)|, |\Delta\Phi_{||,b}(t)|)}{e \Delta S_{||}(t)}, & \text{if } \Delta\Phi_{||,b}(t) > 0 \ \& \ \Delta\Phi_{||,a}(t) < 0 \\ -\frac{\min(|\Delta\Phi_{||,a}(t)|, |\Delta\Phi_{||,b}(t)|)}{e \Delta S_{||}(t)}, & \text{if } \Delta\Phi_{||,b}(t) < 0 \ \& \ \Delta\Phi_{||,a}(t) > 0 \\ 0, & \text{otherwise} \end{cases} \quad (5.4)$$

where $\Delta\Phi_{||,a}$ is the change in the parallel potential drop above the satellite, estimated from the electrons, between adjacent measurements, $\Delta\Phi_{||,b}$ is the change in

the parallel potential drop below the satellite, estimated from the ions, between adjacent measurements and ΔS_{\parallel} the distance along the flux tube which the satellite has traveled. This offers a more reliable, though more conservative estimate of the parallel electric fields.

5.3 Determining the satellite's position relative to the auroral acceleration region

The location of the auroral acceleration region is highly variable and closely dependent on the properties of the surrounding plasma. As discussed in Section 3.7, as electrons on closed field lines move closer to the Earth, magnetic mirroring causes the number of electrons which can carry the upward current to decrease. In order to maintain current continuity, a parallel electric field is required to overcome the effects of magnetic mirroring. For this reason the altitude of the acceleration region varies with the ambient electron density. In the dayside magnetosphere, photo-ionization causes the electron density to be enhanced compared to the nightside magnetosphere. As a consequence, the dayside acceleration region is typically located 1.0–1.5 R_E higher than on the nightside. This makes the geocentric altitude an unsuitable reference frame when studying density variations in both individual density cavities as well as when comparing different density cavities.

For events with predominant quasi-static acceleration, one solution to this problem is to adopt a reference frame which describes the spacecraft's position relative to the auroral acceleration region rather than relative to the Earth. One such reference frame is the pseudo altitude, which is estimated from the distribution of the parallel potential drop above and below the satellite. In its most fundamental form, the pseudo altitude, h_{pseudo} , can be written as,

$$h_{pseudo} = \frac{\Phi_{\parallel,b}}{\Phi_{\parallel,a} + \Phi_{\parallel,b}}, \quad (5.5)$$

where $\Phi_{\parallel,a}$ is the parallel potential drop above the spacecraft and $\Phi_{\parallel,b}$ the parallel potential drop below the spacecraft. Following this convention a pseudo altitude of 0 represents a position at the bottom of the acceleration region and a pseudo altitude of 1 the top of the acceleration region.

The implementation of the pseudo altitude can vary depending on which methods are used to estimate the parallel potential drops. The most direct method for estimating the parallel potential drops is to calculate the characteristic energy of the accelerated, (anti-) field aligned, particle populations, as outlined in Section 5.2.

It is worth noting that the estimations of the parallel potential drop above the spacecraft, given by the electron spectrograms, typically are more robust. The first reason for this is that PEACE has a higher energy resolution than CIS. The second reason is that the electrons cross the acceleration region much faster than the ions. In the time it takes the slower ions to pass through the acceleration

region, the potential structure may change so that the characteristic energy of the ions no longer reflects the true parallel potential drop. In contrast, the electrons can be considered a snapshot of the parallel potential drop at that moment. If the integrated perpendicular electric field is used to estimate the parallel potential drop below the spacecraft this effect becomes more pronounced.

In practice, it can often be preferential to implement the pseudo altitude as starting at the top of the auroral acceleration region and subtracting what amounts to a "pseudo depth", which increases the utilization of the more robust electron data without changing the underlying interpretation of the pseudo altitude. This method has been used throughout the four papers included in this thesis and the two different implementations of the pseudo altitude. The distinction between the local and the global pseudo altitude arises from how the two pseudo altitudes are normalized. The local pseudo altitude can be written as,

$$h_{local}(t) = 1 - \frac{\Phi_{||,a}(t)}{\Phi_{||,a}(t) + \Phi_{||,b}(t)}. \quad (5.6)$$

As can be seen from Equation 5.6, the local pseudo altitude is normalized using the local total parallel potential drop. This causes the local pseudo altitude be re-normalized between each pair of parallel potential drop measurements. In contrast, the global pseudo altitude utilizes a single, global normalization, applied to all data points. The global pseudo altitude can be written as,

$$h_{global}(t) = 1 - \frac{\Phi_{||,a}(t)}{max(\Phi_{||,a} + \Phi_{||,b})}. \quad (5.7)$$

In this case, the normalization is performed using the maximum total potential drop observed in the event. For simple auroral arcs, corresponding to an ideal box-shaped potential structure, the global pseudo altitude will often produce the best results. Since the normalization is performed using a single set of measurements any errors introduced in the normalization process will be systematic over the entire auroral arc. In general, this makes the results easier to interpret.

However, the global pseudo altitude is not ideal when the total potential drop exhibits large variations. This could for example occur near the edges of the auroral arc due to the gradual closure of equipotential lines. Similarly, employing global pseudo altitude can lead to unrealistic results when applied to more complex potential structures such as those of double arcs or large systems of arcs. In this case the local pseudo altitude may be a more suitable choice. The local normalization is better at taking into account changes in the total potential drop but may introduce significant non-systematic errors which can make its interpretation less straightforward. A more detailed description of the interpretation of the global pseudo altitude can be found in Paper 1, Section 2.1.1.

5.4 Estimating currents

The magnetic field data from the FGM can be used to estimate currents using one of Maxwell's equations,

$$\mathbf{j} = \frac{1}{\mu_0} \nabla \times \mathbf{B}, \quad (5.8)$$

where μ_0 is the permeability of vacuum and \mathbf{B} the magnetic field (Paschmann and Daly, 2008). For three or more satellites a generalized solution can be employed. The current density through the plane spanned by three satellites can be estimated from Equation 5.8 by assuming that the magnetic field variations between the satellites are linear. As illustrated in Figure 5.1, adding a fourth satellite, creating a tetrahedral formation, allows for estimating the full three dimensional current from three of the tetrahedron's faces and use the fourth face to provide a sanity check by verifying current continuity and that $\nabla \cdot \mathbf{B}$ is zero, or close to zero.

Under such ideal circumstances, this offers the possibility to reconstruct the full three dimensional current vector. However, the accuracy is highly dependent on the satellite's formation. Geometries that deviate from the ideal tetrahedron will lower the accuracy significantly. In addition, the satellite separation must be small enough, compared to the typical scale size of the current structures, so that the assumption of linear variations in the magnetic field will hold. The Cluster mission has focused on achieving this geometry around the magnetopause and reconnection regions of the magnetotail. Therefore, the crossings of the auroral region does generally not offer opportunities for this type of current estimations.

In the auroral region the current can instead be estimated by using the infinite current sheet approximation. The approximation, which usually is applicable in the auroral region, assumes that the satellite crosses a one dimensional sheet of field aligned current which has an infinite extent. This allows us to reduce Equation 5.8 to a simpler form,

$$\mathbf{j}_{\parallel} = \frac{1}{\mu_0} \frac{\partial \mathbf{B}_{\perp}}{\partial \mathbf{x}_{\mathbf{n}}}, \quad (5.9)$$

where \mathbf{B}_{\perp} is the magnetic field perpendicular to the current sheet and $\partial \mathbf{x}_{\mathbf{n}}$ is the satellite's motion in the direction normal to the current sheet. The main drawback is that the accuracy of the estimate is highly dependent on the validity of the infinite current sheet approximation. Estimating the orientation of the current sheet, relative to the satellite's motion, offers an important validity check of the infinite current sheet approximation. For single satellite events this can be performed using a number of minimum/maximum variance methods, such as: maximum variance of electric field (MVAE), minimum variance of magnetic field (MVAB) or minimum Faraday residue (MFR). For multiple satellite events this can be achieved through various forms of discontinuity analysis, with or without, support from the previously mentioned single satellite methods (Paschmann and Daly, 2000).

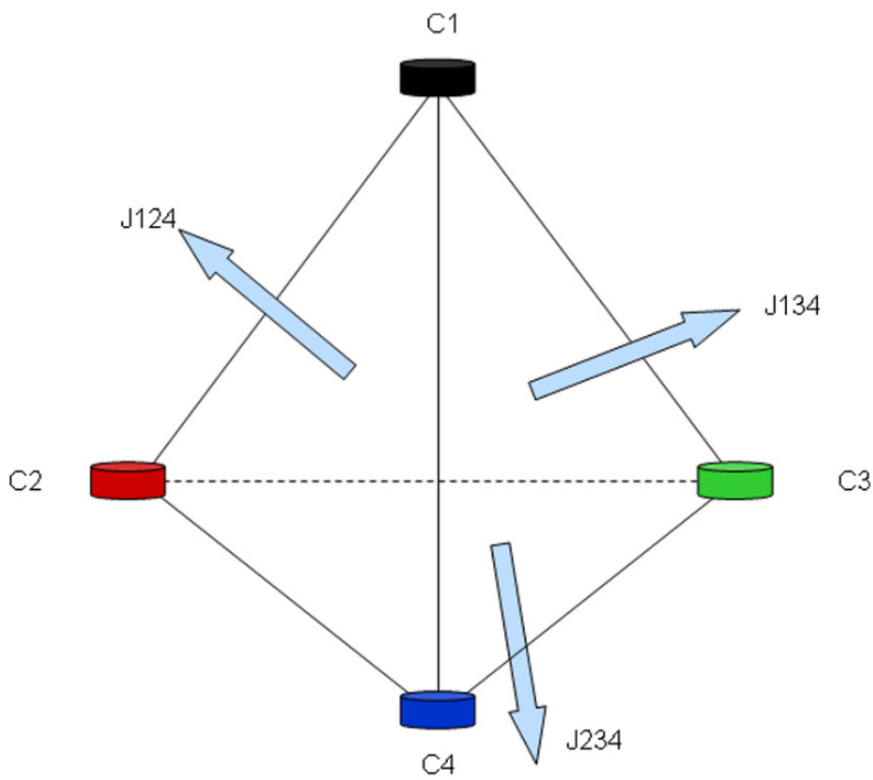


Figure 5.1: The curlometer method using the four satellites. From Grimald *et al.* (2012)

Chapter 6

Results

An initial study, testing the feasibility of using the pseudo altitude as a tool for characterizing the electron density distribution of the auroral density cavity, was conducted using Cluster data from 2008. The data set consisted of seven events, located between 2.6 and 4.0 R_E geocentric altitude. As can be seen in Figure 6.1, an overall trend for decreasing electron densities could be seen with increasing geocentric altitude. This is to be expected as the ambient plasma density decreases with altitude. However, this overall decrease in electron density is much smaller than the electron density variations seen in the individual events. In addition, the geocentric altitude struggles to describe the electron density variations of individual events. The density variations that are observed in the individual events are mainly due to the transverse motion of the satellite rather than the small change in altitude.

Describing the electron density variations as a function of the pseudo altitude paints a different picture. As can be seen in Figure 6.2, all of the events exhibits an anti-correlation between the electron density and pseudo altitude. In each of the events, the lower range of electron densities is consistently found at the highest pseudo altitudes. Three events exhibited a pseudo altitude in excess of 0.95, associated with electron densities lower than 0.1 cm^{-3} . This indicated that these density cavities extended close to the upper edge of the acceleration region.

The relative contributions of quasi-static acceleration and Alfvénic acceleration on cavity formation have been the topic of some discussion. Alfvénic acceleration is a well-known phenomenon in the auroral region and can cause parallel particle acceleration to energies which are comparable to that of quasi-static acceleration. We found that Alfvénic acceleration tended to suppress cavity formation. For comparable pseudo altitudes the electron density could be as much as half an order of magnitude higher in the presence of Alfvénic activity. This is in agreement with previous studies on the subject (Marklund *et al.*, 2011).

Subsequent in-situ observations have shown that the lower part of the auroral density cavity exhibits a highly asymmetric parallel electric field. The ionospheric side of the boundary between the ionosphere and the cavity was well defined and

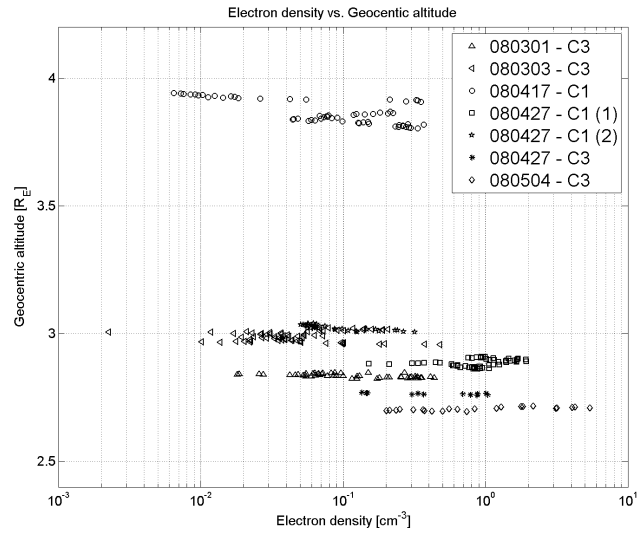


Figure 6.1: Summary plot of the electron density as a function of geocentric altitude. From Alm *et al.* (2013)

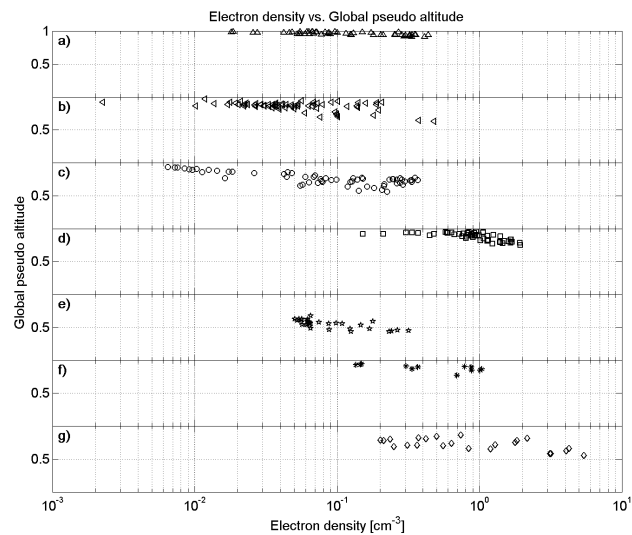


Figure 6.2: Summary plot of the electron density as a function of pseudo altitude. From Alm *et al.* (2013)

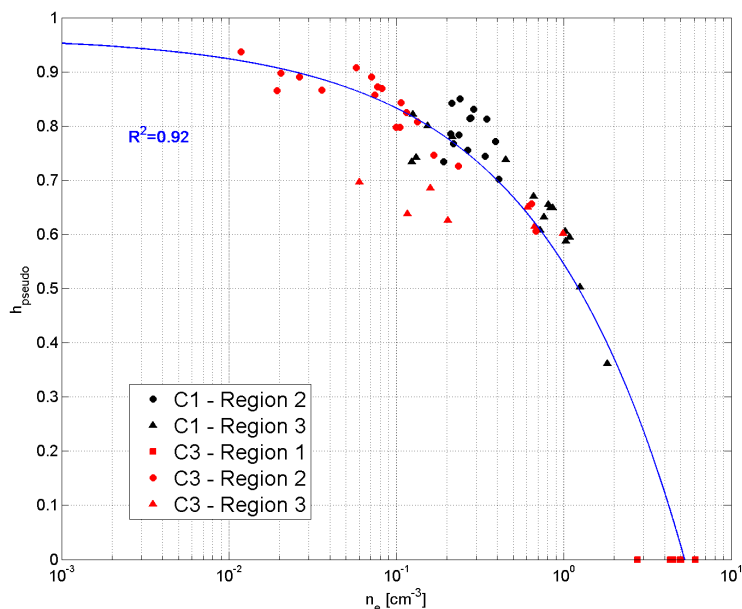


Figure 6.3: Electron density versus local pseudo altitude. Black circles are C1 region 2, black triangles are C1 region 3, red squares are C3 region 1, red circles are C3 region 2 and red triangles are C3 region 3. The solid blue line represents the best fit of the Kappa density distribution, where R^2 is the coefficient of determination. From Alm *et al.* (2015b)

associated with strong ($>400\text{mV/m}$) parallel electric fields and a two orders of magnitude density decrease over a distance of 11 km. The cavity side of the boundary exhibited a weak, $< 20\text{ mV/m}$, distributed electric field and gradual density decrease extending over $>100\text{ km}$. The combination of direct observations of the lower edge of the density cavity by satellite C3 and observations of the mid-cavity by satellite C1 allowed us to create the most comprehensive electron density profile to date, with a combined pseudo altitude coverage of 0–0.95. As can be seen in Figure 6.3, the electron density and pseudo altitude is anti-correlated throughout the entire pseudo altitude range, 0 to 0.95. The data shows that the electron density distribution as a function of the pseudo altitude is reminiscent of a planar sheath, formed out of a plasma sheet dominated electron population, in response to the parallel electric field of the auroral acceleration region.

In-situ observations of the Cluster satellites encountering the upper edge of the acceleration region has allowed us to determine if the density cavity can extend

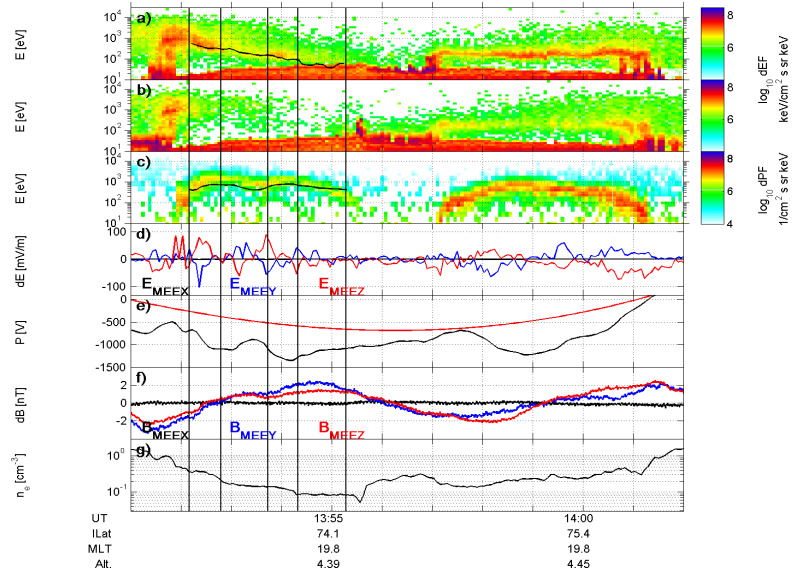


Figure 6.4: Summary plot showing C1 crossing the upper edge of the AAR. (a) downgoing electrons, (b) upgoing electrons, (c) upward ions, (d) the electric field, (e) electric potential, (f) perturbations of the magnetic field, (g) electron density. From Alm *et al.* (2014)

all the way to the top of the acceleration region. As can be seen in Figure 6.4, the electron density exhibited a correlation with the characteristic energy of the inverted-V electrons, equivalent to an anti-correlation with the pseudo altitude, decreasing as the satellite moved closer to the upper edge of the acceleration region. At 13:54:14 UT, satellite C1 could no longer observe inverted-V electrons, while the ion beam remained, indicating that the satellite had crossed above the upper edge of the acceleration region, but remained inside the same flux tube. This coincided with a sharp decrease in the electron density which remained low until the satellite left the flux tube of the acceleration region. The minimum electron density of the density cavity was observed shortly after the satellite crossed the upper edge of the acceleration region. Satellite C1 observed an average parallel electric field of 11.4 mV/m with a peak value of 29.5 mV/m, while satellite C3 observed an average parallel electric field of 8.5 mV/m with a peak parallel electric field of 42.7 mV/m. The associated parallel potential drop accounted for 20–25 % of the total parallel potential drop.

Using the spacecraft potential as a proxy for the electron density has allowed us access to more data compared to relying on calibrations using WHISPER’s electron

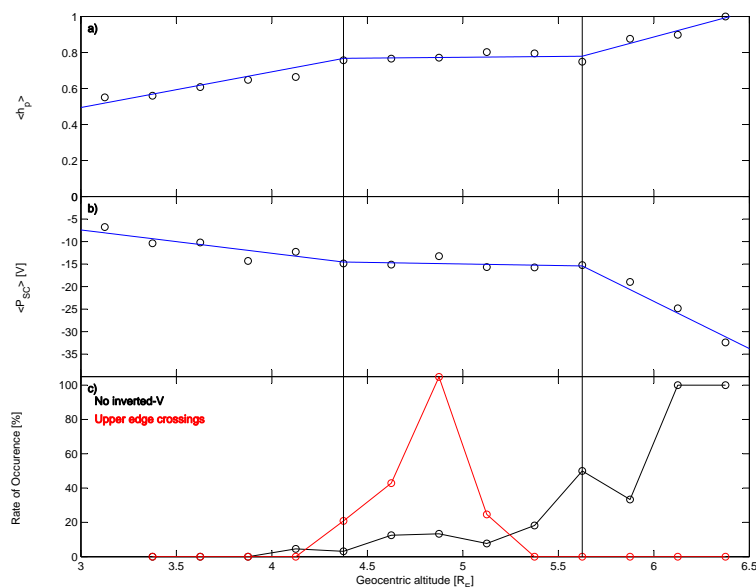


Figure 6.5: Summary plot of statistical extent and distribution of the auroral density cavities. (a) pseudo altitude, (b) spacecraft potential, (c) events where the satellite is located at the upper edge of the auroral acceleration region (red) or above the upper edge of the acceleration region (black). From Alm *et al.* (2014)

density data. This has allowed us to study the electron density distribution of the auroral density cavity in a statistical sense. We identified all instances, during the years 2002–2007, when satellites C1 and C3 were located inside flux tubes containing auroral acceleration. Since the auroral acceleration region typically extends below the geocentric altitude range in question, 3.0–6.5 R_E , such events could be identified from the presence of an upward ion beam. Events in which the upper edge of the acceleration region could be observed or where the satellite was located above the acceleration region could be identified from the electron spectrograms. The pseudo altitude was calculate for the time exhibiting the highest total parallel potential drop, typically near the center of the cavity, and the spacecraft potential was recorded. The resulting data on spacecraft potential and pseudo altitude was binned according to the geocentric altitude.

The results, which are presented in Figure 6.5, exhibits three well defined altitude regions. Between 3.0 and 4.375 R_E geocentric altitude the spacecraft potential decreased by $-5.2/R_E$ and the pseudo altitude increased by 0.2 per R_E . Between

4.375 and 5.625 R_E geocentric altitude, both the spacecraft potential and pseudo altitude only exhibited minor changes. The spacecraft potential decreased by -0.7 V/R_E and the pseudo altitude increases by 0.01 per R_E . Between 5.625 and 6.5 R_E geocentric altitude, the spacecraft potential decreased by -21 V/R_E and the pseudo altitude increased by 0.28 per R_E . The majority of the direct observations of the upper edge of the acceleration occurred between 4.375 and 5.625 R_E geocentric altitude, with a peak rate of occurrence at 4.875 R_E geocentric altitude. In addition, the rate of occurrence of events located entirely above the acceleration region increased with the geocentric altitude. Above a geocentric altitude of 6 R_E , all of the events were located above the acceleration region.

Chapter 7

Discussion and Conclusions

A commonly used picture of the auroral density cavity is that it is confined inside the auroral acceleration by a double layer at the ionosphere-cavity boundary and a double layer at the cavity-magnetosphere boundary (Ergun *et al.*, 2002a, 2004). In effect, the upper and lower edges of the density cavity are thought to coincide with the upper and lower edges of the acceleration region.

Our observations support the picture that the lower edge of the acceleration region does coincide with the lower edge of the acceleration region. The nature of the parallel electric field is as of yet undetermined. The parallel potential drop and strong electric fields on the ionospheric side of the boundary are in agreement with simulations of double layer (Ergun *et al.*, 2000, 2002a). However, the region of weak parallel electric field has a larger extent, over 100 km into the density cavity, than is supported by classic double layer, or with simulations of asymmetric double layers (Ergun *et al.*, 2004). In contrast, quasi-neutral solutions could explain the extended region of parallel electric fields, but would typically not be able to explain the strong parallel electric fields on the ionospheric side of the boundary (Chiu and Schultz, 1978).

The mid-cavity has been proposed to contain the parallel electric field required to maintain quasi-neutrality, either in the form of a mid-cavity double layers (Ergun *et al.*, 2004), or a distributed parallel electric field (Mozer and Hull, 2001). The weak, < 20 mV/m, parallel electric field which were observed inside the density cavity are not in agreement with simulations of mid-cavity double layers, which are associated with parallel potential drops on the order of 1.5–5 keV and parallel electric fields on the order of 300 mV/m (Main *et al.*, 2013).

The statistical data support the idea that the top of the acceleration region could consist of a discrete region of parallel electric field. However, the weak, < 50 mV/m, parallel electric field and small parallel potential drop are not consistent with a double layer. The parallel electric field is in agreement with an ambipolar field supported by the vertical density gradient, indicating that it could be one possible mechanism. However, there is not sufficient data to draw any conclusions

on the exact nature of the mechanism supporting the parallel electric field.

Both individual events and the statistical data support the conclusion that the electron density is anti-correlated with the pseudo altitude. This implies that the electron density decrease as we move higher up into the acceleration region. This anti-correlation has been found to hold for all pseudo altitudes, with no indications of the electron density increasing at higher pseudo altitudes. The lowest electron densities are consistently observed at the highest pseudo altitudes. This anti-correlation holds above $6.0 R_E$, where the satellites only observe density cavities located above the acceleration region. We have as of yet not been able to observe the upper edge of an auroral density cavity within the geocentric altitude range of 3.0 – $6.5 R_E$. The data does not support idea that the upper edge of the density cavity coincides with the upper edge of the acceleration region (Ergun *et al.*, 2002a, 2004).

Many previous studies have concluded that the auroral acceleration region is a phenomenon which is typically found at geocentric altitudes between 2 and $3 R_E$ (Karlsson *et al.*, 2012). However, our results indicate that the auroral acceleration region may extend over a larger altitude range than previously thought and have a more complicated structure. Figure 7.1, is a model which summarizes our current understanding of the structure of the auroral density cavity in relation to the auroral acceleration region. As illustrated by the distribution of the lines of constant electric potential, we expect that a significant portion of the total parallel potential drop to be located above a geocentric altitude of $3 R_E$. A geocentric altitude which often has been considered the upper boundary of the acceleration region. The majority of our observations of the upper edge of the acceleration region were located between a geocentric altitude of 4.375 and $5.725 R_E$, with no events in which the satellite was located inside the acceleration region observed above $6 R_E$. This indicates that on average the auroral acceleration region on average extends some 1 – $2 R_E$ higher than previously assumed. Similar results have been found in previous statistical studies, though based on a smaller number of events. As can be seen in Figure 7.2, between 25 – 50 % of the parallel potential drop occurred above a geocentric altitude of $3 R_E$, with the last 10 – 15 % observed above a geocentric altitude of $4 R_E$ (Mozer and Hull, 2001). The reoccurring observations of density cavities extending above the acceleration region and lack of observations of the upper edge of the cavity indicates that it may extend to much higher altitudes than previously thought, possibly down tail to the plasma sheet.

Our findings show that the auroral density cavity and auroral acceleration region are closely interconnected. Not only is the density cavity a prominent feature of the auroral acceleration region, but its density distribution appears to be a direct response to the distribution of the auroral parallel electric fields. The electron density distribution observed by satellite C1 and C3 (Figure 6.3), are consistent despite a large difference in total parallel potential drop and field aligned current observed by the two satellites, This illustrates the utility of employing pseudo altitude as a frame of reference when studying the auroral density cavity.

Our results highlight that the auroral density cavity and auroral acceleration

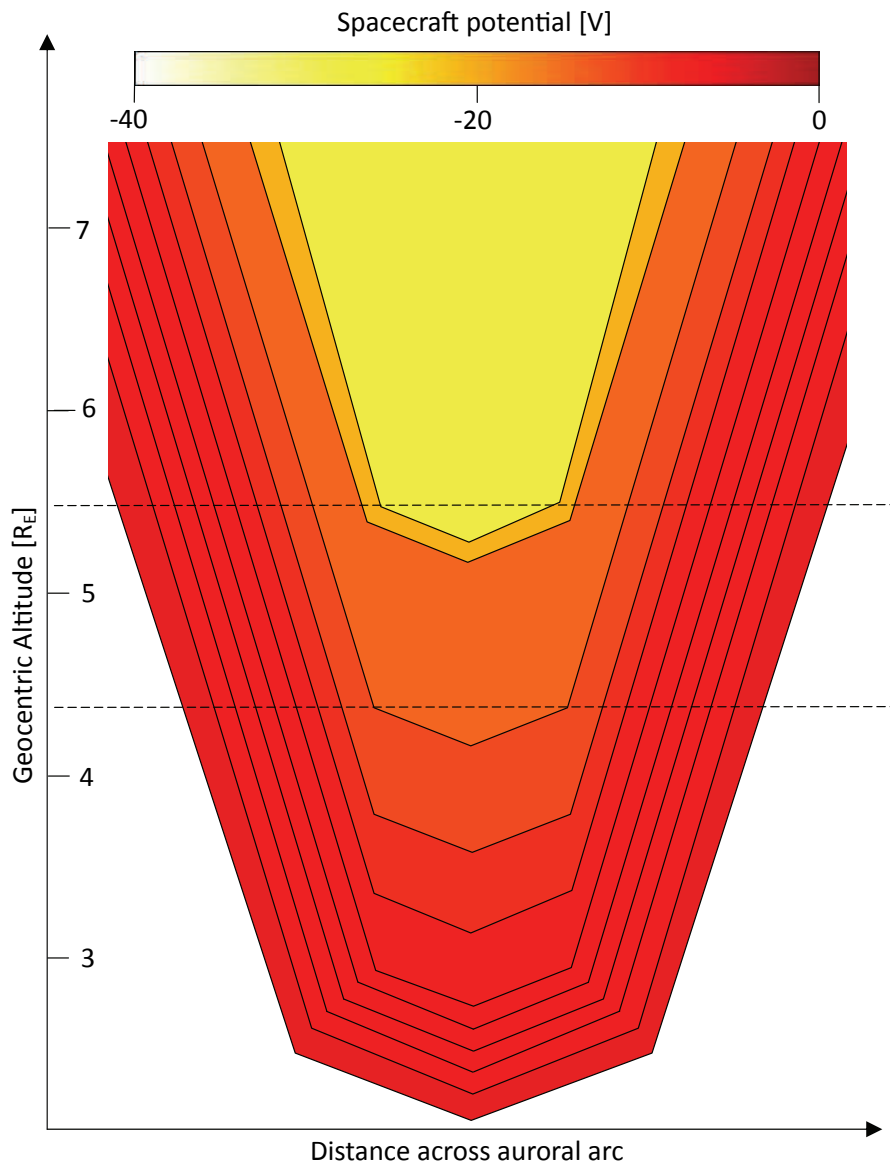


Figure 7.1: Model of potential structure and density cavity based on the statistical data. The solid lines represent lines of constant electric potential, equivalent to lines of constant pseudo altitude with a resolution of 0.1. The region bound by the horizontal dashed lines is where the upper edge of the AAR is observed. The color scale is the mean spacecraft potential. From Alm *et al.* (2015a)

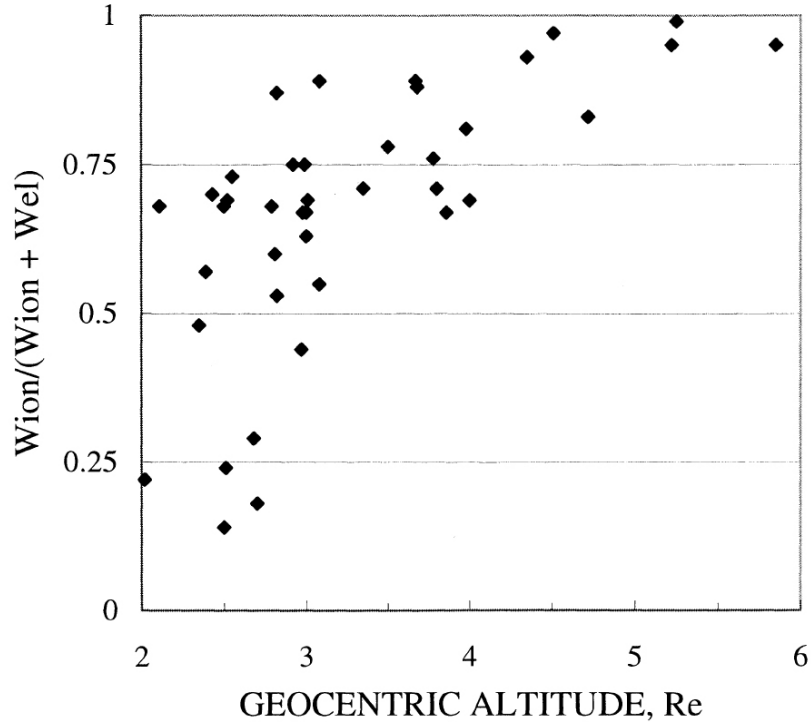


Figure 7.2: Distribution of electron and ion energy as a function of geocentric altitude. The quantity of the y-axis is the equivalent of the local pseudo altitude. Adapted from Mozer and Hull (2001)

region should be studied in a unified fashion. In addition, the various regions of the acceleration region appear to be more closely connected than indicated by previous observational studies and simulations.

Fully understanding how the density distribution of the auroral density cavity arises will likely require a combination of additional in-situ observations of the auroral density cavity and auroral acceleration region as well as a better understanding of the initial conditions before the formation of the cavity. This would likely require a satellite mission dedicated to studying auroral physics. Such a mission, *Alfén+* was proposed as an ESA medium-class mission but was not selected as a candidate for the final round. Cluster's spiritual successor, the MMS constellation, will not cover the auroral region. The constellation has a low inclination orbit, focusing on studying the microphysics of magnetic reconnection, at the magnetopause and in the magnetotail. However, it may give important insights into the mechanism which provides the energy driving the aurora.

Understanding the underlying mechanism supporting the parallel electric fields and generating the density cavity will likely require dedicated modelling efforts. Future computer models of the auroral density cavity and auroral acceleration region should strive to model the entire cavity as one entity, as opposed to piecewise modelling of the various regions. This appears to be especially true for the low altitude and mid-cavity parallel electric fields. The strong interdependence between the parallel electric field and electron density distribution indicates that static models may be highly sensitive to the chosen initial state. Setting the initial state may force solutions which are not suitable representations of the auroral region. Long duration models, describing the formation of the acceleration region and density cavity from ambient conditions, are likely required to fully understand the underlying mechanisms. Such large scale and long duration models will be computationally intense and may require other analytical methods than those utilized in previous models.

Bibliography

- S.-I. Akasofu. 1964. The development of the auroral substorm. *Planetary and Space Science*, 12(4):273 – 282. ISSN 0032-0633. URL <http://www.sciencedirect.com/science/article/pii/0032063364901515>.
- H. Alfvén. 1955. On the electric field theory of magnetic storms and aurorae. *Tellus*, 7(1):50–64. ISSN 2153-3490. URL <http://dx.doi.org/10.1111/j.2153-3490.1955.tb01140.x>.
- Hannes Alfvén. 1950. *Cosmic Electrodynamics*, 1 edition. The International series of monographs on physics. Clarendon Press.
- L. Alm, B. Li, G. T. Marklund, and T. Karlsson. 2015a. Statistical altitude distribution of the auroral density cavity. *Journal of Geophysical Research: Space Physics*, 120(2):996–1006. ISSN 2169-9402. URL <http://dx.doi.org/10.1002/2014JA020691>.
- L. Alm, G. T. Marklund, and T. Karlsson. 2014. In situ observations of density cavities extending above the auroral acceleration region. *Journal of Geophysical Research: Space Physics*, pages n/a–n/a. ISSN 2169-9402. URL <http://dx.doi.org/10.1002/2014JA019799>.
- L. Alm, G. T. Marklund, and T. Karlsson. 2015b. Electron density and parallel electric field distribution of the auroral density cavity. *Journal of Geophysical Research: Space Physics (forthcoming)*.
- L. Alm, G. T. Marklund, T. Karlsson, and A. Masson. 2013. Pseudo altitude: A new perspective on the auroral density cavity. *Journal of Geophysical Research: Space Physics*. ISSN 2169-9402. URL <http://dx.doi.org/10.1002/jgra.50408>.
- A. Balogh, M.W. Dunlop, S.W.H. Cowley, D.J. Southwood, J.G. Thomlinson, K.H. Glassmeier, G. Musmann, H. Lühr, S. Buchert, M.H. Acuña, D.H. Fairfield, J.A. Slavin, W. Riedler, K. Schwingenschuh, and M.G. Kivelson. 1997. The cluster magnetic field investigation. *Space Science Reviews*, 79(1-2):65–91. ISSN 0038-6308. URL <http://dx.doi.org/10.1023/A%3A1004970907748>.
- W. Baumjohann. 1997. *Basic Space Plasma Physics*. Imperial College Press. ISBN 978-1860940798.

- Jeffrey Bennet, Megan Donahue, Nicholas Schneider, and Mark Voit. 2008. *The Essential Cosmic Perspective: Media Update; 4th ed.* Addison-Wesley, San Francisco, CA. URL <https://cds.cern.ch/record/1095030>. Accompanies Astronomy Media Workbook.
- R. Benson and W. Calvert. 1979. ISIS 1 observations at the source of auroral kilometric radiation. *Geophys. Res. Lett.*, 6(6):479–482.
- Robert F Benson, Wynne Calvert, and David M Klumpar. 1980. Simultaneous wave and particle observations in the auroral kilometric radiation source region. *Geophysical Research Letters*, 7(11):959–962.
- Lars P Block. 1972. Potential double layers in the ionosphere. *Cosmic Electrodyn*, 3(3):349–376.
- W. Calvert. 1981. The auroral plasma cavity. *Geophys. Res. Lett.*, 8(8):919–921.
- C. Carr, P. Brown, N. Alconcel, T. Oddy, and P. Fox. 2014. *User Guide to the FGM measurements in the Cluster Active Archive (CAA)*, 6.0 edition. WHISPER team.
- C. C. Chaston, V. Genot, J. W. Bonnell, C. W. Carlson, J. P. McFadden, R. E. Ergun, R. J. Strangeway, E. J. Lund, and K. J. Hwang. 2006. Ionospheric erosion by Alfvén waves. *Journal of Geophysical Research: Space Physics*, 111(A3). ISSN 2156-2202. URL <http://dx.doi.org/10.1029/2005JA011367>.
- Francis F. Chen. 2006. *Introduction to Plasma Physics and Controlled Fusion*, volume 1. Springer Science. ISBN 987-0-306-41332-2.
- Y. T. Chiu and M. Schultz. 1978. Self-consistent particle and parallel electrostatic field distributions in the magnetospheric-ionospheric auroral region. *Journal of Geophysical Research: Space Physics*, 83(A2):629–642.
- I. Dandouras and A. Barthe. 2014. *User Guide to the CIS measurements in the Cluster Active Archive (CAA)*, 3.4 edition. CIS Team.
- Paola De Michelis, Ioannis A Daglis, and Giuseppe Consolini. 1997. Average terrestrial ring current derived from ampte/cce-chem measurements. *Journal of Geophysical Research: Space Physics (1978–2012)*, 102(A7):14103–14111.
- P.M.E. Décréau, P. Fergeau, V. Krannosels’kikh, M. Lévêque, Ph. Martin, O. Randriamboarison, F.X. Sené, J.G. Trotignon, P. Canu, and P.B. Mørgensen. 1997. Whisper, a resonance sounder and wave analyser: Performances and perspectives for the cluster mission. *Space Science Reviews*, 79(1-2):157–193. ISSN 0038-6308. URL <http://dx.doi.org/10.1023/A%3A1004931326404>.
- Eric E Dors and Craig A Kletzing. 1999. Effects of suprathermal tails on auroral electrodynamics. *Journal of Geophysical Research: Space Physics (1978–2012)*, 104(A4):6783–6796.

- N Dunckel, B Ficklin, L Rorden, and BA Helliwell. 1970. Low-frequency noise observed in the distant magnetosphere with ogo 1. *Journal of Geophysical Research Space Physics*, 75(10).
- R. E. Ergun, L. Andersson, D. Main, Y.-J. Su, D. L. Newman, M. V. Goldman, C. W. Carlson, A. J. Hull, J. P. McFadden, and F. S. Mozer. 2004. Auroral particle acceleration by strong double layers: the upward current region. *J. Geophys. Res.*, 109(A12220).
- R. E. Ergun, L. Andersson, D. Main, Y.-J. Su, D. L. Newman, M. V. Goldman, C. W. Carlson, J. P. McFadden, and F. S. Mozer. 2002a. Parallel electric fields in the upward current region of the aurora: Numerical solutions. *Physics of Plasmas*, 9(9):3695–3704.
- R. E. Ergun, L. Andersson, D. S. Main, Y.-J. Su, C. W. Carlson, J. P. McFadden, and F. S. Mozer. 2002b. Parallel electric fields in the upward current region of the aurora: Indirect and direct observations. *Physics of Plasmas (1994-present)*, 9(9):3685–3694. URL <http://scitation.aip.org/content/aip/journal/pop/9/9/10.1063/1.1499120>.
- R. E. Ergun, C. W. Carlsson, J. P. McFadden, F. S. Mozer, and R. J. Strangeway. 2000. Parallel electric fields in discrete arcs. *Geophys. Res. Let.*, 27(24):4053–4056.
- CP Escoubet, Rüdiger Schmidt, and Christopher Russell. 2012. *The Cluster and PHOENIX missions*. Springer Science & Business Media.
- A. N. Fazakerley. 2014. *User Guide to the PEACE measurements in the Cluster Active Archive (CAA)*, 2.5 edition. PEACE Operations Team.
- U Feldman, E Landi, and NA Schwadron. 2005. On the sources of fast and slow solar wind. *Journal of Geophysical Research: Space Physics (1978–2012)*, 110(A7).
- S. Grimald, I. Dandouras, P. Robert, and E. Lucek. 2012. Study of the applicability of the curlometer technique with the four cluster spacecraft in regions close to earth. *Annales Geophysicae*, 30(3):597–611. URL <http://www.ann-geophys.net/30/597/2012/>.
- D. A. Gurnett. 1974. The earth as a radio source: Terrestrial kilometric radiation. *J. Geophys. Res.*, 79(28):4227–4238.
- G. Gustafsson, R. Boström, B. Holback, G. Holmgren, A. Lundgren, K. Stasiewicz, L. Åhlén, F.S. Mozer, D. Pankow, P. Harvey, P. Berg, R. Ulrich, A. Pedersen, R. Schmidt, A. Butler, A.W.C. Fransen, D. Klinge, M. Thomsen, C.-G. Fälthammar, P.-A. Lindqvist, S. Christenson, J. Holtet, B. Lybekk, T.A. Sten, P. Tanskanen, K. Lappalainen, and J. Wygant. 1997. The electric field and wave

- experiment for the cluster mission. *Space Science Reviews*, 79:137–156. ISSN 0038-6308.
- G. Haerendel, H. U. Frey, O. H. Bauer, E. Rieger, J. Clemmons, M. H. Boehm, D. D. Wallis, and H. L $\frac{1}{4}$ hr. 1994. Inverted-v events simultaneously observed with the freja satellite and from the ground. *Geophysical Research Letters*, 21(17): 1891–1894. ISSN 1944-8007. URL <http://dx.doi.org/10.1029/94GL01692>.
- M. K. Hudson and F. S. Mozer. 1978. Electrostatic shocks, double layers, and anomalous resistivity in the magnetosphere. *Geophysical Research Letters*, 5(2):131–134. ISSN 1944-8007. URL <http://dx.doi.org/10.1029/GL005i002p00131>.
- A. J. Hull, J. W. Bonnell, F. S. Mozer, and J. D. Scudder. 2003. A statistical study of large-amplitude parallel electric fields in the upward current region of the auroral acceleration region. *Journal of Geophysical Research: Space Physics*, 108(A1):SMP 5–1–SMP 5–23. ISSN 2156-2202. URL <http://dx.doi.org/10.1029/2001JA007540>.
- A. J. Hull, M. Wilber, C. C. Chaston, J. W. Bonnell, J. P. McFadden, F. S. Mozer, M. Fillingim, and M. L. Goldstein. 2010. Time development of field-aligned currents, potential drops, and plasma associated with an auroral poleward boundary intensification. *Journal of Geophysical Research: Space Physics*, 115(A6). ISSN 2156-2202. URL <http://dx.doi.org/10.1029/2009JA014651>.
- Bengt Hultqvist, Marit Øieroset, Goetz Paschmann, and Rudolf Treumann, editors. 1999. *Magnetospheric plasma sources and losses*, 1 edition. Space Sciences Series of ISSI. Springer Netherlands. ISBN 978-0-7923-5846-6.
- Takesi Iijima and Thomas A Potemra. 1978. Large-scale characteristics of field-aligned currents associated with substorms. *Journal of Geophysical Research: Space Physics (1978–2012)*, 83(A2):599–615.
- P. Janhunen and A. Olsson. 1998. The current-voltage relationship revisited: exact and approximate formulas with almost general validity for hot magnetospheric electrons for bi-maxwellian and kappa distributions. *Annales Geophysicae*, 16(3): 292–297. URL <http://www.ann-geophys.net/16/292/1998/>.
- P. Janhunen, A. Olsson, and H. Laakso. 2002. Altitude dependence of plasma density in the auroral zone. *Annales Geophysicae*, 20(11):1743–1750. URL <http://www.ann-geophys.net/20/1743/2002/>.
- Charles Y Johnson. 1969. Ion and neutral composition of the ionosphere. *Annals of the IQSY*, 5:197–213.
- A.D. Johnstone, C. Alsop, S. Burge, P.J. Carter, A.J. Coates, A.J. Coker, A.N. Fazakerley, M. Grande, R.A. Gowen, C. Gurgiolo, B.K. Hancock, B. Narheim,

- A. Preece, P.H. Sheather, J.D. Winningham, and R.D. Woodliffe. 1997. Peace: A plasma electron and current experiment. *Space Science Reviews*, 79:351–398. ISSN 0038-6308.
- Tomas Karlsson, Nils Brenning, H. Nilsson, J-G Trotignon, X. Vallières, and G. Facsko. 2012. Localized density enhancements in the magnetosheath : Three-dimensional morphology and possible importance for impulsive penetration. *Journal of Geophysical Research*, 117:A03227–. QC 20120507.
- L. Kepko, R.L. McPherron, O. Amm, S. Apatenkov, W. Baumjohann, J. Birn, M. Lester, R. Nakamura, T.I. Pulkkinen, and V. Sergeev. 2014. Substorm current wedge revisited. *Space Science Reviews*, pages 1–46. ISSN 0038-6308. URL <http://dx.doi.org/10.1007/s11214-014-0124-9>.
- Margaret G. Kivelson and Christopher T. Russell. 1995. *Introduction to Space Physics*. Cambridge University Press. ISBN 978-0-521-45104-8.
- C. A. Kletzing, J. D. Scudder, E. E. Dors, and C. Curto. 2003. Auroral source region: Plasma properties of the high-latitude plasma sheet. *Journal of Geophysical Research: Space Physics*, 108(A10):n/a–n/a. ISSN 2156-2202. URL <http://dx.doi.org/10.1029/2002JA009678>.
- Stephen Knight. 1973. Parallel electric fields. *Planetary and Space Science*, 21(5): 741–750.
- DJ Knipp, BA Emery, M Engebretson, X Li, AH McAllister, T Mukai, S Kokubun, GD Reeves, D Evans, T Obara, *et al.* 1998. An overview of the early november 1993 geomagnetic storm. *Journal of Geophysical Research: Space Physics (1978–2012)*, 103(A11):26197–26220.
- Hannu EJ Koskinen and Eija I Tanskanen. 2002. Magnetospheric energy budget and the epsilon parameter. *Journal of Geophysical Research: Space Physics (1978–2012)*, 107(A11):SMP–42.
- Harri Laakso, Matthew G.T.T. Taylor, and C. Philippe Escoubet, editors. 2010. *The Cluster Active Archive*. Springer. ISBN 978-90-481-3498-4.
- B. Li, G. Marklund, L. Alm, T. Karlsson, P.-A. Lindqvist, and A. Masson. 2014. Statistical altitude distribution of cluster auroral electric fields, indicating mainly quasi-static acceleration below 2.8 RE and Alfvénic above. *Journal of Geophysical Research: Space Physics*, 119(11):8984–8991. ISSN 2169-9402. URL <http://dx.doi.org/10.1002/2014JA020225>. 2014JA020225.
- Bin Li, Göran Marklund, Tomas Karlsson, Soheil Sadeghi, Per-Arne Lindqvist, Andris Vaivads, Andrew Fazakerley, Yongliang Zhang, Elizabeth Lucek, Tima Sergienko, *et al.* 2013. Inverted-v and low-energy broadband electron acceleration features of multiple auroras within a large-scale surge. *Journal of Geophysical Research: Space Physics*, 118(9):5543–5552.

- P.-A. Lindqvist, C. Cully, and Y. Khotyaintsev. 2014. *User Guide to the EFW measurements in the Cluster Active Archive (CAA)*, 3.5 edition. EFW team.
- G. Lu, P. H. Reiff, J. L. Burch, and J. D. Winningham. 1991. On the auroral current-voltage relationship. *Journal of Geophysical Research: Space Physics (1978–2012)*, 96(A3):3523–3531.
- D. S. Main, D. L. Newman, and R. E. Ergun. 2006. Double layers and ion phase-space holes in the auroral upward-current region. *Phys. Rev. Lett.*, 97:185001. URL <http://link.aps.org/doi/10.1103/PhysRevLett.97.185001>.
- D. S. Main, D. L. Newman, and R. E. Ergun. 2010. Conditions for establishing quasistable double layers in the earth’s auroral upward current region. *Physics of Plasmas*, 17(12):122901. URL <http://link.aip.org/link/?PHP/17/122901/1>.
- D. S. Main, D. L. Newman, C. Scholz, and R. E. Ergun. 2013. The formation and evolution of double layers inside the auroral cavity. *Geophysical Research Letters*, 40(12):2897–2901. ISSN 1944-8007. URL <http://dx.doi.org/10.1002/grl.50608>.
- G. T. Marklund, S. Soheil, J. A. Cumnock, T. Karlsson, P.-A. Lindqvist, H. Nilsson, A. Masson, A. Fazakerley, E. Lucek, and Y. Zhang. 2011. Evolution in space and time of the quasi-static acceleration potential of inverted-V aurora and its interaction with Alfvénic boundary processes. *J. Geophys. Res.*, 116. doi:10.1029/2011JA016537.
- Göran T Marklund, Soheil Sadeghi, Bin Li, O Amm, Judy A Cumnock, Y Zhang, H Nilsson, A Masson, Tomas Karlsson, P-A Lindqvist, *et al.* 2012. Cluster multipoint study of the acceleration potential pattern and electrodynamics of an auroral surge and its associated horn arc. *Journal of Geophysical Research: Space Physics (1978–2012)*, 117(A10).
- J. P. McFadden, C. W. Carlson, R. E. Ergun, D. M. Klumpar, and E. Moebius. 1999. Ion and electron characteristics in auroral density cavities associated with ion beams: No evidence for cold ionospheric plasma. *J. Geophys. Res.*, 104(A7):14,671–14,682.
- Robert L. McPherron. 1970. Growth phase of magnetospheric substorms. *Journal of Geophysical Research*, 75(28):5592–5599. ISSN 2156-2202. URL <http://dx.doi.org/10.1029/JA075i028p05592>.
- DB Melrose, KG Rönnmark, and RG Hewitt. 1982. Terrestrial kilometric radiation: The cyclotron theory. *Journal of Geophysical Research: Space Physics (1978–2012)*, 87(A7):5140–5150.
- F. S. Mozer, C. W. Carlson, M. K. Hudson, R. B. Torbert, B. Parady, J. Yatteau, and M. C. Kelley. 1977. Observations of paired electrostatic shocks in the polar magnetosphere. *Phys. Rev. Lett.*, 38:292–295.

- F. S. Mozer and A. Hull. 2001. Origin and geometry of upward parallel electric fields in the auroral acceleration region. *J. Geophys. Res.*, 106(A4):5763–5778.
- F. S. Mozer and C. A. Kletzing. 1998. Direct observation of large, quasi-static, parallel electric fields in the auroral acceleration region. *Geophys. Res. Lett.*, 25(10):1629–1632.
- A. Olsson and P. Janhunen. 1998. Field-aligned conductance values estimated from maxwellian and kappa distributions in quiet and disturbed events using freja electron data. *Annales Geophysicae*, 16(3):298–302. URL <http://www.ann-geophys.net/16/298/1998/>.
- G. Paschmann, S. Haaland, and R. Treumann, editors. 2003. *Auroral Plasma Physics*. Space Sciences Series of ISSI. Kluwer Academic Publishers.
- Götz Paschmann and Patrick W. Daly, editors. 2000. *Analysis Methods for Multi-Spacecraft Data*. ISSI / ESA Publications Division.
- Götz Paschmann and Patrick W. Daly, editors. 2008. *Multi-Spacecraft Analysis Methods Revisited*. ISSI / ESA Communications. ISBN 987-92-9221-937-6.
- A. Pedersen, B. Lybakk, M. André, A. Eriksson, A. Masson, F. S. Mozer, P.-A. Lindqvist, P. M. E. Décréau, I. Dandouras, J.-A. Sauvaud, *et al.* 2008. Electron density estimations derived from spacecraft potential measurements on cluster in tenuous plasma regions. *J. Geophys. Res.*, 113(A7):A07S33.
- A. M. Persoon, D. A. Gurnett, W. K. Peterson, J. H. Waite, J. L. Burch, and J. L. Green. 1988. Electron density depletions in the nightside auroral zone. *J. Geophys. Res.*, 93(A3):1871–1895.
- GW Pneuman and Roger A Kopp. 1971. Gas-magnetic field interactions in the solar corona. *Solar Physics*, 18(2):258–270.
- H. Rème, J.M. Bosqued, J.A. Sauvaud, A. Cros, J. Dandouras, C. Aoustin, J. Bouyssou, Th. Camus, J. Cuvilo, C. Martz, J.L. Médale, H. Perrier, D. Romefort, J. Rouzaud, C. D’Uston, E. Möbius, K. Crocker, M. Granoff, L.M. Kistler, M. Popecki, D. Hovestadt, B. Klecker, G. Paschmann, M. Scholer, C.W. Carlson, D.W. Curtis, R.P. Lin, J.P. Mcfadden, V. Formisano, E. Amata, M.B. Bavassano-Cattaneo, P. Baldetti, G. Belluci, R. Bruno, G. Chionchio, A. Di Lellis, E.G. Shelley, A.G. Ghielmetti, W. Lennartsson, A. Korth, H. Rosenbauer, R. Lundin, S. Olsen, G.K. Parks, M. Mccarthy, and H. Balsiger. 1997. The cluster ion spectrometry (CIS) experiment. *Space Science Reviews*, 79:303–350. ISSN 0038-6308.
- Kenneth H. Schatten, John M. Wilcox, and Norman F. Ness. 1969. A model of interplanetary and coronal magnetic fields. *Solar Physics*, 6(3):442–455. ISSN 0038-0938. URL <http://dx.doi.org/10.1007/BF00146478>.

- J. D. Scudder, C. Xuejun, and F. S. Mozer. 2000. Photoemission current-spacecraft coltage relation: Key to routine, quantitative low-energy plasma measurements. *J. Geophys. Res.*, 105(A9):21281–21894.
- Y. Song and R. L. Lysak. 2001. Towards a new paradigm: from a quasi-steady description to a dynamical description of the magnetosphere. *Space Science Reviews*, 95(1-2):273–292.
- M. Temerin, K. Cerny, W. Lotko, and FS Mozer. 1982. Observations of double layers and solitary waves in the auroral plasma. *Physical Review Letters*, 48(17):1175.
- J.G. Trotignon and X. Vallières. 2014. *User Guide to the WHISPER measurements in the Cluster Active Archive (CAA)*, 1.4 edition. WHISPER team.
- David R. Williams. 2015. Sun fact sheet. <http://nssdc.gsfc.nasa.gov/planetary/factsheet/sunfact.html>.
- CS Wu and LC Lee. 1979. A theory of the terrestrial kilometric radiation. *The Astrophysical Journal*, 230:621–626.